ADVANCING EARTH AND SPACE SCIENCES

JGR Oceans

RESEARCH ARTICLE

10.1029/2025JC023905

The Structure and Lifecycle of Stratified Mixing by Shear Instabilities in Continuously Forced Flows

Adrien Lefauve[1,2], C. Bassett[3], D. S. Plotnick[4], A. C. Lavery[5], and W. R. Geyer[6]

[1]Grantham Institute – Climate Change and the Environment, Imperial College London, London, UK, [2]Department of Civil and Environmental Engineering, Imperial College London, London, UK, [3]Applied Physics Laboratory, University of Washington, Seattle, WA, USA, [4]Applied Research Laboratory, Pennsylvania State University, State College, PA, USA, [5]College of Earth, Ocean and Atmospheric Sciences, Oregon State University, Corvallis, OR, USA, [6]Applied Ocean Physics and Engineering Department, Woods Hole Oceanographic Institution, Woods Hole, MA, USA

Key Points:

- Ocean stratified mixing hotspots sustained by shear below marginal instability follow an energy cascade not controlled by overturning
- At high Reynolds number, observations and modeling show that mixing occurs in thin braids where secondary instability triggers turbulence
- A baroclinic production-dissipation balance predicts mixing across scales, with laboratory data revealing filamentary mixing within braids

Correspondence to:

A. Lefauve,
a.lefauve@imperial.ac.uk

Citation:

Lefauve, A., Bassett, C., Plotnick, D. S., Lavery, A. C., & Geyer, W. R. (2026). The structure and lifecycle of stratified mixing by shear instabilities in continuously forced flows. *Journal of Geophysical Research: Oceans*, *131*, e2025JC023905. https://doi.org/10.1029/2025JC023905

Received 17 DEC 2025
Accepted 8 JUN 2026

Author Contributions:

Conceptualization: Adrien Lefauve, W. R. Geyer
Data curation: Adrien Lefauve, C. Bassett, D. S. Plotnick, W. R. Geyer
Formal analysis: Adrien Lefauve, W. R. Geyer
Funding acquisition: Adrien Lefauve, A. C. Lavery, W. R. Geyer
Investigation: Adrien Lefauve
Methodology: Adrien Lefauve, D. S. Plotnick, A. C. Lavery, W. R. Geyer
Project administration: Adrien Lefauve
Resources: Adrien Lefauve, A. C. Lavery, W. R. Geyer
Software: Adrien Lefauve, C. Bassett, D. S. Plotnick
Supervision: Adrien Lefauve, W. R. Geyer
Validation: Adrien Lefauve, C. Bassett, D. S. Plotnick, W. R. Geyer
Visualization: Adrien Lefauve

Abstract

The turbulent energy cascade of ocean mixing remains poorly understood at geophysically large Reynolds numbers (Re). Here we propose a new conceptual model for the structure of small-scale mixing grounded in high-resolution multibeam echosounding observations from the mouth of the Connecticut River, a shallow salt-wedge estuary. Tidal forcing and bottom topography slope the pycnocline, sustaining interfacial shear and Kelvin–Helmholtz instabilities well below the marginal instability threshold on a vertical scale of order 1 m. Acoustic backscatter, used here as a proxy for salinity microstructure dissipation, provides time-resolved two-dimensional imagery of the structure and evolution of turbulent mixing. At Re $\sim 10^6$, we find that mixing is dominated not by the collapse of slowly evolving billow cores as at Re $\sim 10^3-10^4$, but instead by fast turbulence within the ~ 0.1 m thin, shallow-sloping braids that connect them, energized by baroclinic shear. We interpret these observations using two-dimensional direct numerical simulation at field-matched parameters, which predicts the emergence of secondary Kelvin–Helmholtz instabilities and turbulence within the braids, pre-empting further steepening and primary overturn. We then estimate turbulent dissipation and scalar variance dissipation at the pycnocline and braid scales using physics-based scalings involving only the local slope, shear and layer thickness. Laboratory experiments in an inclined duct, an analog of the turbulent braid regime, visualize mixing down to dissipative scales, where it remains organized in myriad thin, sheared, intense filaments rather than overturns. We conclude that high-Re mixing hotspots with sustained shear forcing follow fundamentally different dynamics than previously thought.

Plain Language Summary

The mixing of different water layers is not well understood, despite being central to how heat, salt, oxygen, and nutrients move through natural waters. Intense turbulent mixing often occurs in localized regions created by strong flows, such as tides near river mouths. Here we study this process using high-resolution sonar observations from the Connecticut River estuary. Our measurements produce detailed images of underwater waves and the thin, fast-moving layers between them. These layers act somewhat like the steep face a surfer rides, but we show that they rarely steepen enough to form a large overturning roller at their crest. Instead, their slopes generate many smaller turbulent structures that do the mixing. Computer simulations reproducing the observed conditions support this picture, physical modeling predicts the strength of the mixing from simple properties of the flow, and laboratory experiments in a sloping channel let us zoom in on the turbulence itself. Our results differ from smaller-scale instabilities, where mixing is often concentrated inside the main overturning billows, and may improve predictions in other vigorous ocean and coastal flows.

1. Introduction

Diapycnal turbulent mixing is one of the cornerstones of ocean dynamics. The way mixing regulates the vertical transport and thus the distribution of temperature, salinity and tracers (e.g., carbon, nutrients) has far-reaching implications for ocean and climate physics (Melet et al., 2022). Since the ocean is mostly stably-stratified, small-scale turbulence is often initiated by shear instabilities—typically Kelvin–Helmholtz instabilities—triggered when the background vertical shear $S = |\partial \bar{u}/\partial z|$ exceeds twice the background buoyancy frequency $N = \sqrt{\partial \bar{b}/\partial z}$, that is when the gradient Richardson number satisfies

$$\mathrm{Ri} = \frac{N^2}{S^2} < \frac{1}{4}, \tag{1}$$

Writing – original draft: Adrien Lefauve
Writing – review & editing: Adrien Lefauve, C. Bassett, A. C. Lavery, W. R. Geyer

which is referred to as the Miles-Howard criterion for parallel shear flow (Howard, 1961; Miles, 1961). These instabilities, and the stratified turbulence that ensues, are a key energy pathway linking internal waves and other submesoscales (above 100 m or so) to three-dimensional turbulence (below 0.1 m or so) (D'Asaro, 2022; Smyth & Moum, 2012; Taylor & Thompson, 2023).

Certain environments are continually forced, meaning that the stratification and shear persist long enough to sustain repeated cycles of shear instability and turbulent mixing. These hotspots include straits (Wesson & Gregg, 1994), the equatorial undercurrent (Smyth et al., 2013), deep overflows (Cusack et al., 2019), deep seamounts (van Haren & Gostiaux, 2010), shallow seamounts (Vladoiu et al., 2025) and estuaries (Geyer et al., 2010). These hotspots not only contribute to large-scale water mass transformation and energy budgets (Cimoli et al., 2023; Waterhouse et al., 2014) but also shape local circulation patterns, chemistry and biology (Hasegawa et al., 2021; Hoecker-Martínez & Smyth, 2012; Steinbuck et al., 2009) and can feed back on climate modes such as the El Niño–Southern Oscillation (Liu et al., 2025) due to their high levels of turbulent kinetic dissipation ϵ and buoyancy variance dissipation χ defined as

$$\epsilon = 2\nu \|\mathbf{s}'\|^2 \quad \text{and} \quad \chi = \frac{D}{N^2} |\nabla b'|^2. \tag{2}$$

Here $\mathbf{s}' = \left(\nabla \mathbf{u}' + \nabla \mathbf{u}'^T\right)/2$ is the strain-rate tensor of the perturbation velocity field $\mathbf{u}'$, ν is the kinematic viscosity of seawater, D is the molecular diffusivity of the buoyancy perturbation field b' due to the underlying salinity or temperature variations. For single-scalar stratification, χ can serve as a proxy for irreversible diapycnal mixing (Taylor et al., 2019, Equation 8), (Caulfield, 2020, Sec. II.C). In addition to being energetically important, these continuously forced environments are ideal to study shear instabilities. Understanding the spatial structure and temporal evolution (lifecycle) of these shear instabilities is crucial to build physics-based parameterizations of their non-hydrostatic effects in regional and global ocean models.

Yet, despite their importance, detailed observations of shear instabilities remain relatively rare (e.g., Geyer et al., 2010; Vladoiu et al., 2025). Figure 1 shows an example of high-resolution observation, which will be analyzed in more detail in this paper. Figure 1a shows a 300 m long transect at the mouth of the Connecticut River, along the thalweg, where shear is sustained between the river discharge and the incoming flood tide. This transect was collected by an echosounder in an autonomous underwater vehicle (AUV) (Remote Environmental Monitoring UnitS, REMUS) cruising 2 m below the surface. The signal displayed is acoustic volume scattering strength, which is proportional to $\log_{10}\chi_s$, where

$$\chi_s = 2D_s |\nabla s'|^2 \tag{3}$$

is the dissipation rate of salinity variance at molecular scales. High scattering (yellow shades) therefore serves as a proxy for high irreversible diapycnal mixing (Lavery et al., 2013; details in Section 2.2). Figures 1b and 1c zoom in on shear instabilities on various scales. This paper will focus on the large-scale instabilities found in the mid-water column at the main pycnocline, shown in Figure 1c. This train of KH instabilities grows spatially along the direction of the mean flow from right to left. It appears to be triggered by a tidal intrusion front (Simpson & Nunes, 1981) following the bottom slope of 0.02 (see panel a) and displays an identical mean slope of 0.02 (panel c). (The smaller, steeper train of KH instabilities in panel b appears at the edge of a near-surface shear layer). The bright coherent yellow signal in panel (c) indicates regions of elevated turbulent mixing, as discussed in Section 4.

Such observational data inform us about where and when turbulent dissipation and its associated mixing are strongest. Until now, this understanding was built using insights from idealized direct numerical simulations (DNS) (e.g., Mashayek & Peltier, 2011; Smyth et al., 2001) and laboratory experiments (e.g., Thorpe, 1971, 1973) at moderate Reynolds numbers $\mathrm{Re} = UH/\nu \sim 10^3$–$10^4$, where U and H are representative velocity and length scales. At these Re, the KH billows grow, break turbulently, mix, and then decay due to the lack of forcing. By contrast, the estuarine regime in Figure 1 has a higher $\mathrm{Re} \sim 10^6$ and is continuously forced. This is significant for two reasons. First, Re controls the transition to turbulence and the emergence of smaller secondary instabilities (Caulfield & Peltier, 2000; Mashayek & Peltier, 2012a), which set the turbulent length scales and the history of mixing (Caulfield, 2021). Second, forcing controls the energetics: in continuously forced stratified shear flows—and in other dissipative systems governed by a threshold (here $\mathrm{Ri} = 1/4$)—the rates of kinetic energy and

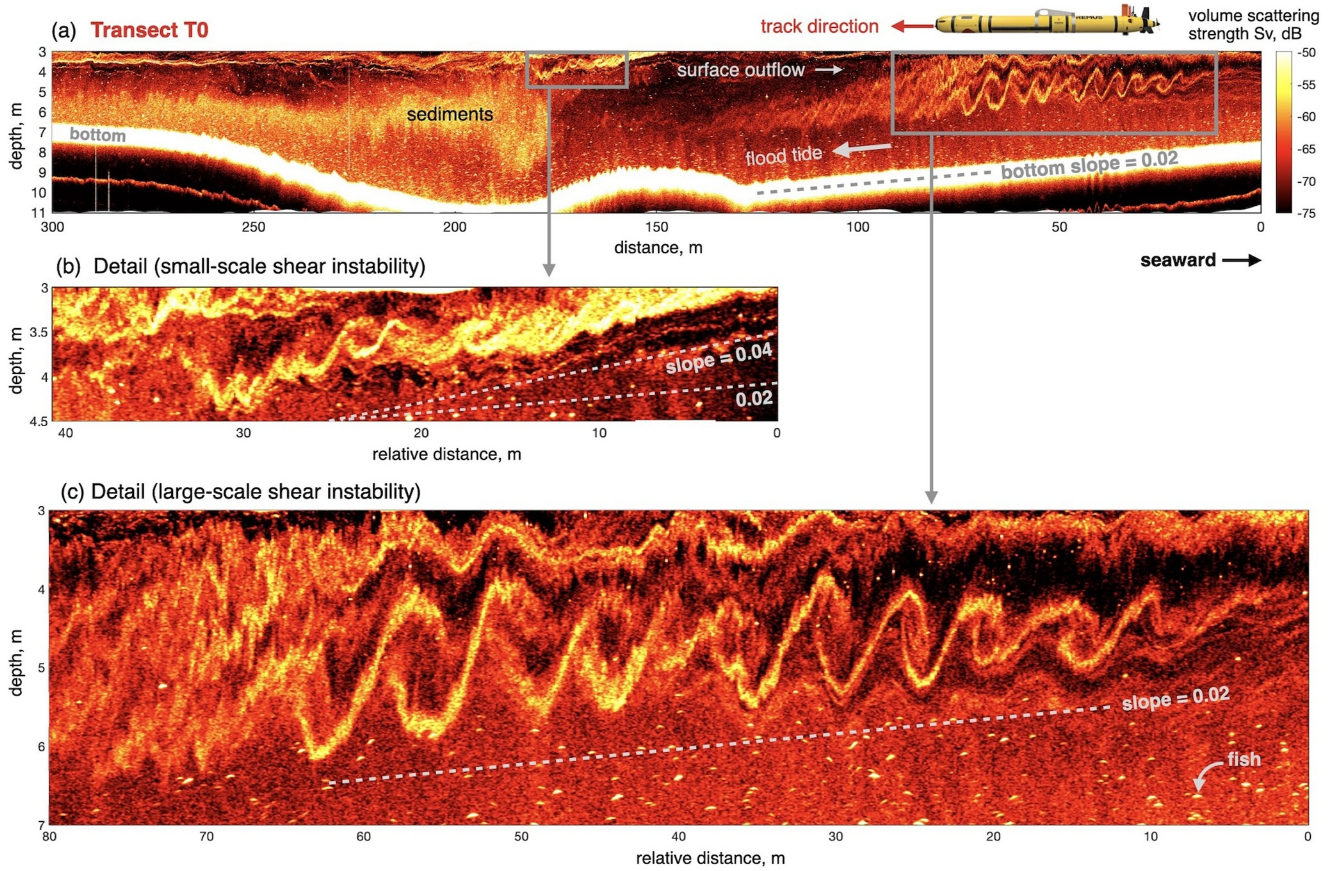

Figure 1. Visualization of turbulent mixing caused by shear instabilities from the acoustic backscatter acquired by an Autonomous Underwater Vehicle (AUV) in the Connecticut River estuary. (a) Whole transect T0 (further details in Figures 2 and 3). AUV not to scale. (b)–(c) Zooming in on details of small-scale (b) and large-scale (c) trains of KH instabilities, the latter one being the main focus of this paper. The vertical exaggeration is 5 in all panels (real slopes are much shallower). The spatial resolution is of order 1 cm in depth and 8 cm along transect. The small bright spots are fish, particularly abundant in the salty bottom layer.

buoyancy variance dissipation (ϵ and χ) balance, on average, the input (e.g., solar heating and trade winds for the equatorial undercurrent; high-latitude cooling and downslope motion for deep overflows; freshwater discharge and tides for estuaries). Shear continuously destabilizes the flow by decreasing Ri below the threshold, while turbulent events restore stability by increasing Ri, producing cycles around an equilibrium value—the state of marginal instability (Smyth, 2020; Thorpe & Liu, 2009; van Haren et al., 1999) which has also been interpreted within the broader framework of self-organized criticality (Bak et al., 1988; Salehipour et al., 2018).

Evidence already exists that the moderate-Re, unforced DNS regime differs from the high-Re, forced regime in the ocean. In DNS, most of the turbulent mixing occurs within the convectively unstable billows ("bright cores"), whereas field observations at Re $\sim 10^6 - 10^8$ (Figure 1c and Geyer et al., 2010; Vladoiu et al., 2025; see also Appendix A) consistently show that mixing concentrates instead in the connecting "bright braids"—thin, high-shear regions linking the weaker "quiet cores." In this paper, we provide new support for this hypothesis articulated in earlier work (Geyer et al., 2010), and develop it into a predictive quantitative model by addressing two major open questions tied to long-standing methodological challenges.

1. What are the spatial structure and lifecycle of these high-mixing zones? Most existing backscatter data, including that shown in Figure 1 and Appendix A, comes from *single-beam* echosounders, meaning that vertical soundings (lines) are aggregated along the track axis, creating two-dimensional images which inevitably suffer from distortions associated with the relative motion between the underwater KH wave (controlled by the depth-varying current) and the instrument. This can either steepen or flatten slopes, and generally entangles spatial and temporal evolutions in ways that are hard to quantify and correct for. Here we overcome

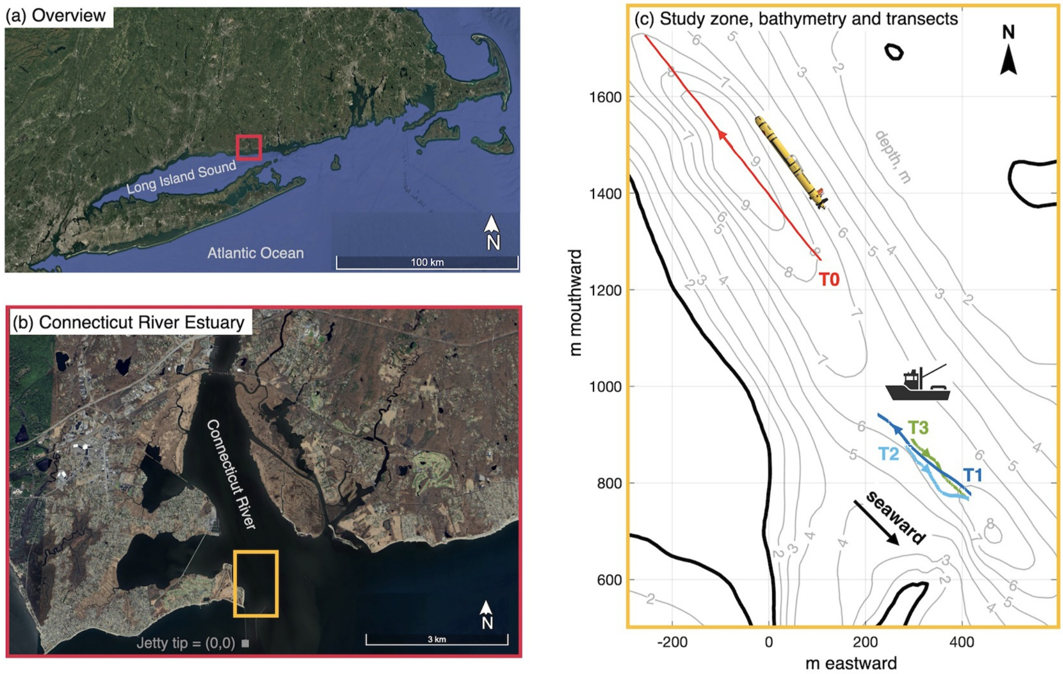

Figure 2. Field site. (a) Location of the Connecticut River estuary (see red box). (b) Zoom in on the mouth of the estuary. Note the study zone (see yellow box) and the jetty tip as reference point with coordinates (0, 0). (c) Bathymetry and transects in the study zone (coordinates are relative to the jetty tip). The four transects investigated in this paper: T0 (AUV-based) and T1–3 (shipboard).

this challenge with a *multibeam* echosounder that disentangles spatial and temporal evolution and captures the fine-scale dynamics of shear-instability mixing down to centimeter scales and tens of milliseconds.

2. How does the turbulent cascade operate within these high-mixing braids, well below the resolution of direct observations, down to sub-mm scale? The high Re values in the ocean allow the KH braids to sharpen down to the cm scale and increase their local shear, triggering secondary instabilities and turbulence. We will use highly-resolved two-dimensional (2D) DNS with parameters matching field values to demonstrate this process and quantify the length- and time scales involved. After the emergence of three-dimensional (3D) braid turbulence at scales of ~ 0.1 m, stratified turbulence theory predicts a downscale cascade with a multi-decade inertial subrange. We will use a relevant laboratory experiment to visualize mixing down to ~ 0.1 mm and quantify turbulence forced by the braid slope using physics-based estimates for ϵ and χ_s from the local slope, shear, and thickness. This will allow us to hypothesize why the primary cores rarely overturn in observations, completing our understanding of the structure and lifecycle of mixing by shear instabilities in continuously forced flows.

To achieve this, Section 2 introduces the observational data, including the field site, instruments, and multibeam echosounding. In addition to the AUV transect from Figure 1, three shipboard transects with co-located acoustics and hydrodynamic data will reveal in Section 3 the forcing mechanism leading to the primary KH instability and the expected separation of scales of turbulence, motivating the next sections. Section 4 delves deeper into the acoustics data, documenting the features of braid turbulence with the multibeam data and comparing them to the single-beam data of Figure 1. Section 5 employs numerical modeling to prove the existence of and characterize secondary braid instabilities before explaining how existing laboratory experiments in an inclined flume are relevant to model the ensuing braid turbulence and mixing. Section 6 concludes and Section 7 gives the broader implications of our findings for ocean mixing.

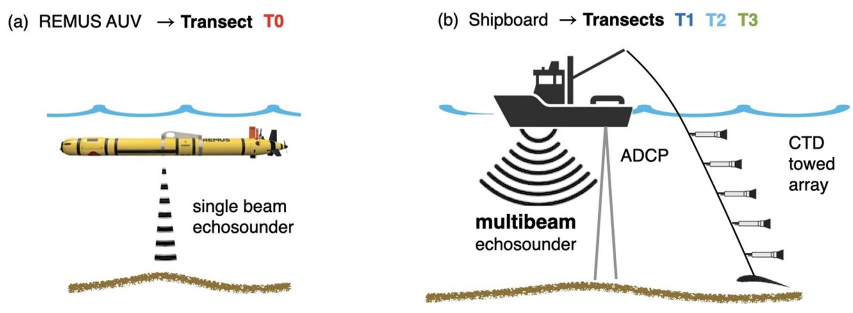

Figure 3. Instrumentation and resulting data sets. (a) The AUV-based transect T0 provides single-beam acoustics. (b) The shipboard transects T1–3 provide multibeam acoustics with current profiles (nearly colocated acoustic Doppler current profiler) and salinity/density profiles (towed CTD, just aft of the vessel).

2. Methods and Overview of Observations

2.1. Site and Instruments

We conducted field observations at the mouth of the Connecticut River estuary (Figures 2a and 2b), focusing on a study region with a natural channel 5–10 m deep with gently sloping bathymetry (Figure 2c). The data set comprises four transects which exhibit a large number of KH instabilities: T0, surveyed with an AUV, already shown in Figure 1, and T1–T3, obtained from shipboard measurements. A moving platform was required because the instability trains evolve spatially along the pycnocline and their location cannot be predicted a priori. The instrumentation is summarized in Figure 3. The AUV (model: REMUS 100) carried a broadband single-beam echosounder operating at 200 kHz nominal frequency (model: Simrad WBTmini with ES200-7CDK transducer, 7° full beamwidth, 100 kHz bandwidth, 1 ms signal) (Bassett et al., 2022). The vessel-mounted equipment included a pole mounted off the starboard side with (a) a multibeam echosounder (Kongsberg M3) operating at 500 kHz with a 20 μs pulse with a nominal resolution of 1.5 cm (Melvin et al., 2012); (b) a co-located acoustic Doppler current profiler (ADCP) providing current data at 0.25 m vertical resolution (Nortek Signature 1,000, operating at 1 MHz); and (c) a towed array of five conductivity–temperature–depth (CTD) sensors spaced 1 m vertically (RBR Concerto, sampling at 17 Hz). Unlike conventional multibeam systems, which are typically oriented cross-track to image the seafloor, ours aligned the transmit–receive swath in the along-track direction, parallel to the vessel's motion (Figure 3b). This fore–aft geometry captured the instabilities along the vessel's path (following the thalweg) in the plane in which they develop, keeping the features in the sonar's field of view for long enough to observe their evolution. The raw multibeam data were rectified to correct for vessel heave, pitch, and roll by combining navigation and motion-sensor data with feature tracking using backscattering from the seabed (for details, see Appendix B). This fine level of multibeam data motion correction is essential for the visualization and interpretation of small-scale coherent structures that follows since even modest changes (e.g., several degrees) in pitch and roll associated with unavoidable vessel motion can significantly shift the apparent location of imaged features. All data sets are available in the repository (Lefauve et al., 2026).

The T0 data were collected on 29 June 2017 (between 16:18:57–16:23:52 UTC, local time = UTC-4), approximately 3.5 hr after slack water (12:55 UTC), during the flood tide. The AUV was cruising 2 m below the surface at a constant speed of 1 m s^{-1}. The T1–3 data were collected a day later on 30 June 2017 (16:05:30–16:33:21 UTC), approximately 2–2.5 hr after slack water (14:05 UTC), also during the flood tide. The vessel speed varied during each transect and between transects, with averages of 1.9 m s^{-1} (T1), 0.45 m s^{-1} (T2) and 0.63 m s^{-1} (T3). Although our data is exclusively during the flood tide, KH instabilities have been previously documented during the ebb tide at the mouth and further upstream (Geyer et al., 2010, 2017; Holleman et al., 2016; Lavery et al., 2013). This estuary, like many others, experiences persistently elevated mixing because of the combination of strong shear and persistent stratification.

In summary, the three shipboard transects (T1–3) provide multibeam acoustic data resolving the structure and lifecycle of shear-instability mixing (details in Section 2.2), together with concurrent current and salinity profiles used to examine the background conditions, forcing, and characteristic turbulent length scales (Sections 2.3 and 3).

2.2. Acoustic Backscatter as a Proxy for Turbulent Mixing

The backscatter measured by our echosounders arises from scattering by small-scale density and sound-speed fluctuations associated with scalar microstructure. In the Connecticut River estuary, where stratification is dominated by strong salinity gradients, this scalar microstructure is primarily salinity-driven. Lavery et al. (2013) developed an analytical model, validated by measurements in this estuary, in which the scattering depends on both the salinity-variance dissipation rate χ_s and the turbulent kinetic energy dissipation rate ϵ. Assuming a turbulent spectrum in the viscous–convective subrange, the volume backscattering cross section per unit volume at a fixed frequency can be expressed as

$$\sigma_V = C_1 \chi_s \epsilon^{-1/2} = C_1 \frac{(2N^2\Gamma_\chi)^{1/2}}{g\beta}\chi_s^{1/2}, \quad \text{where} \quad \Gamma_\chi = \frac{\chi}{\epsilon} = \frac{(g\beta)^2\chi_s}{2N^2\epsilon}. \tag{4}$$

Here C_1 is a constant at a fixed acoustic frequency. The first equality is the acoustic scattering relation and retains the dependence on both scalar microstructure, through χ_s, and turbulence intensity, through ϵ. The second equality follows after introducing the mixing-efficiency closure $\Gamma_\chi = \chi/\epsilon$, together with $\chi = (g\beta)^2\chi_s/(2N^2)$ by definition (see Equations 2 and 3). Here $g = 9.81\ \mathrm{m\,s^{-2}}$ is the acceleration of gravity, and $\beta = 7.5 \times 10^{-4}\ \mathrm{psu^{-1}}$ is the saline contraction coefficient at our temperature of 20°C. If N^2 and Γ_χ are taken as approximately constant, the relation simplifies to $\sigma_V = C_2 \chi_s^{1/2}$, where C_2 is another constant.

In this paper we follow sonar acoustics convention and present results in terms of the volume backscattering strength S_V (units dB re 1 $\mathrm{m^{-1}}$):

$$S_V = 10 \log_{10} \sigma_V = 5 \log_{10} \chi_s + C_3, \tag{5}$$

where C_3 is another constant whose determination would require calibration. Calibration was performed in Lavery et al. (2013) but not in this work due to challenges with the in situ calibration of multibeam systems. Thus, direct inversion of S_V for χ_s is not performed here and there is a scalar offset between the values of S_V presented here and those of calibrated systems. However, the essential point here is that a tenfold increase in the underlying mixing rates χ_s corresponds to a 5 dB increase in the measured S_V. In our data, S_V spans a range of about 20 dB, implying four orders of magnitude variation in χ_s. This inferred dynamic range is consistent with previous observations using a calibrated single-beam system; Lavery et al. (2013, Figure 16b) reported a range $\chi_s \approx 10^{-3}$–$1\ \mathrm{psu^2\ s^{-1}}$ within shear instabilities in the main pycnocline.

The processed multibeam data $S_V(x, z, t)$ are output at 17 Hz with a nominal grid spacing of 4 mm in the x–z plane. The effective physical resolution, however, is estimated to be closer to 1–2 cm in the vertical (Bassett et al., 2023), with slightly finer discrimination in range than in azimuth, especially at depth due to the $\sim 1.6°$ resolution of the fan. In practice, these data can thus confidently resolve structures of order ~5 cm, including turbulent braids, although 3D features at these scales may appear blurred due to noise, finite beamwidth and spanwise averaging.

2.3. Shipboard Transects Overview

The hydrodynamic and acoustic data from transects T1–3 are shown in Figures 4–6. In each figure, the top panel (a) presents the salinity along the transect, obtained by fitting a hyperbolic tangent function to the five-point towed CTD array, which yielded excellent fits. The middle panel shows the ADCP velocity profiles, with river discharge plotted as positive velocities (red) and flood tide as negative velocities (blue), consistent with the convention that seaward flow is left to right. The bottom panel (c) displays the volume scattering strength S_V from the vertical beam of the multibeam, providing an overview consistent with the AUV transect of Figure 1. Full multibeam fields are presented later for selected snapshots (labeled A, B, C, …) in Figure 9, corresponding to shear instabilities captured at maximum amplitude. Supplementary movies in Lefauve et al. (2026) show the full temporal evolution of the multibeam data along each transect.

All three transects show a pycnocline sloping slightly upward seaward under the flood tide (Figures 4–6a). The corresponding region of strongest shear—and hence expected KH instability—is marked by gray and white semi-transparent dots where $\mathrm{Ri} < 0.25$ and $N > 0.15\ \mathrm{s^{-1}}$ (Figures 4–6b and 6c). As the flood tide progresses, the

10.1029/2025JC023905

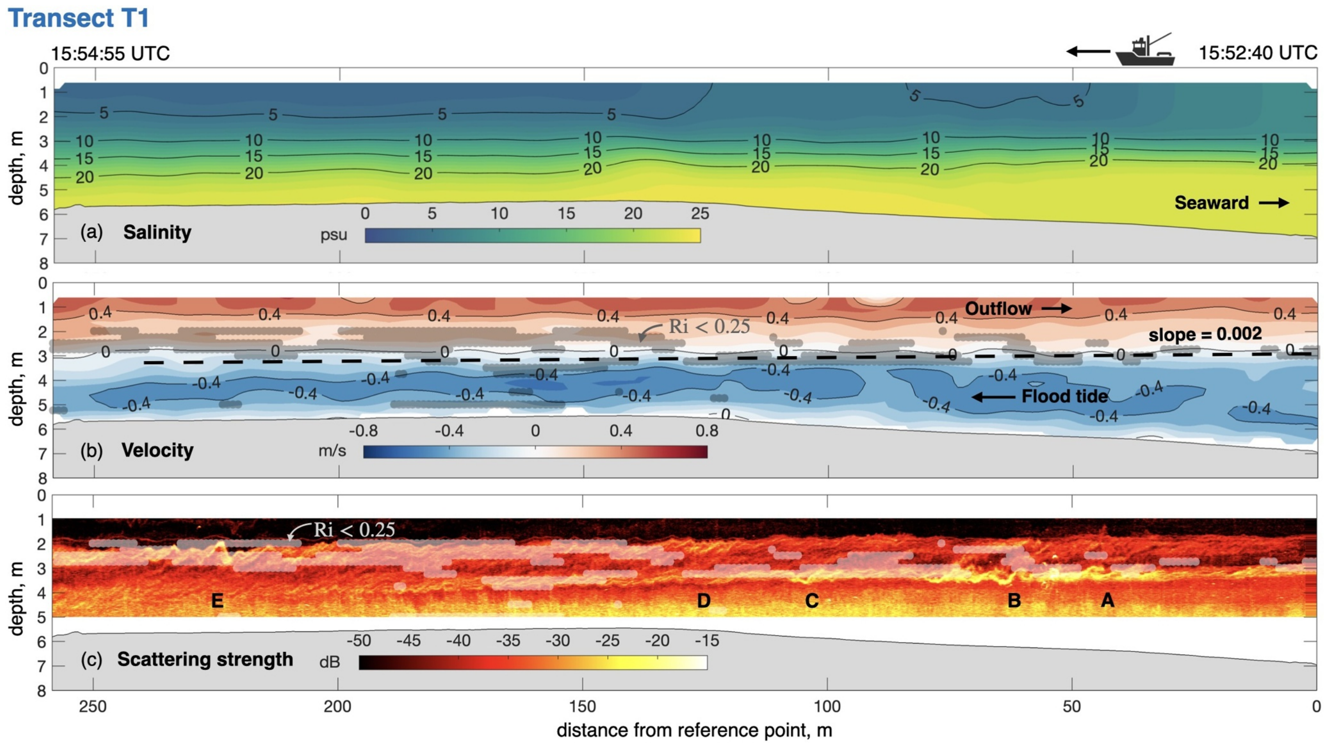

Figure 4. Overview of transect T1, starting 1 hr 47 min after slack water. Track direction is right to left (see the horizontal distance axis). The reference point (distance 0) corresponds to the start of T1 and the end of T2 and T3 (see Figure 2c). Vertical exaggeration is 5 in all panels. (a) Salinity, fitted from the CTD towed array. (b) Velocity from the ADCP (magnitude of the 2D vector $(u^2 + v^2)^{1/2}$, direction indicated by black arrows). (c) Scattering strength, taking only the vertical beam of the multibeam fan. Multibeam snapshots are shown at locations labeled A, B, …, E in Figure 9. In (b), (c) the gray/white symbols are overlaid in regions where $\mathrm{Ri} < 0.25$ and $N > 0.15\ \mathrm{s}^{-1}$ where strong scattering due to turbulent salinity microstructure is expected (and usually found). For plots without overlays, see the repository (Lefauve et al., 2026).

pycnocline and unstable region rise from about 3 m in T1 to 2 m in T3, with a typical slope of ≈ 0.002 (black dashed lines). This region coincides with intense scattering, confirming that mixing occurs where $\mathrm{Ri} < 0.25$.

3. Conditions, Forcing and Energetics of the Primary KH Instability

3.1. Background Conditions

Typical profiles from T2 mid-transect are shown in Figure 7. We plot velocity and salinity (panel a), as well as N, S, and Ri (panel b). We find that the velocity profile exhibits a main inflection point within the pycnocline at 2.5–3 m depth, coinciding with a shear maximum, which are necessary conditions for shear instability (Smyth & Carpenter, 2019). At this depth, the velocity is approximately -0.1 to $-0.2\ \mathrm{m\ s}^{-1}$ (negative, i.e. landward), which also represents the expected propagation speed of KH instability. The gradient Richardson number Ri is likewise robustly below 0.25 here, confirming the possibility of KH instability, although it also drops below this threshold nearer the bottom and surface. As highlighted by the orange rectangle, the maximum scattering due to KH instability observed earlier in Figure 5c occurs at the main inflection point corresponding to the pycnocline rather than in the near-bottom or near-surface layers. This is consistent with Equation 5, since backscatter is a proxy for turbulent mixing (not just turbulence), and both salinity variance and its dissipation are orders of magnitude larger in the pycnocline (identified in this paper by $N > 0.15\ \mathrm{s}^{-1}$). Salinity ranges from ≈ 3 to 23 psu. Notably, the salinity and velocity inflection points are not colocated: the peak in N (corresponding to the mid-pycnocline salinity of 13 psu) is offset ≈ 0.5 m below the peak in S, consistent with previous observations of shear–stratification offsets (van Haren, 2000). This offset makes the KH instability slightly top-down asymmetric.

Figure 8a shows the joint probability distribution of N and S for all transects T1–T3 at depths of 2–4 m, corresponding to the main pycnocline mixing zone. In the unstable region with maximum scattering (the orange triangle below the $\mathrm{Ri} = 0.25$ diagonal line), the typical range is $N \approx 0.15{-}0.3\ \mathrm{s}^{-1}$ and $S \approx 0.4{-}0.8\ \mathrm{s}^{-1}$. A

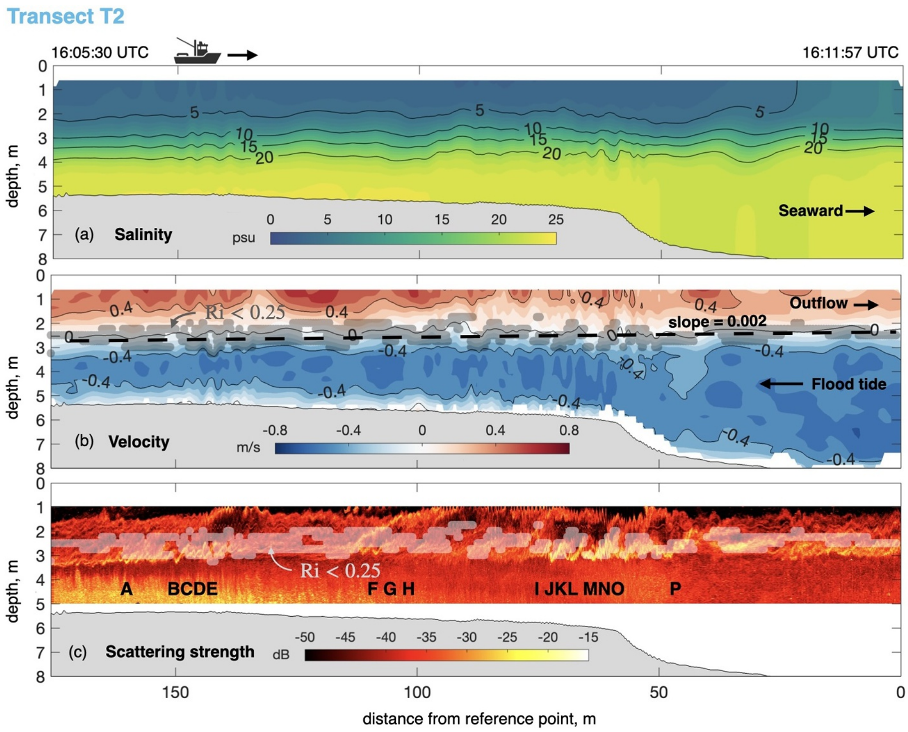

Figure 5. Overview of transect T2, starting 2 hr 0 min after slack water. Track direction is left to right (seaward). Same legend as Figure 4. Multibeam images are shown at locations A, B, … P, in Figure 9.

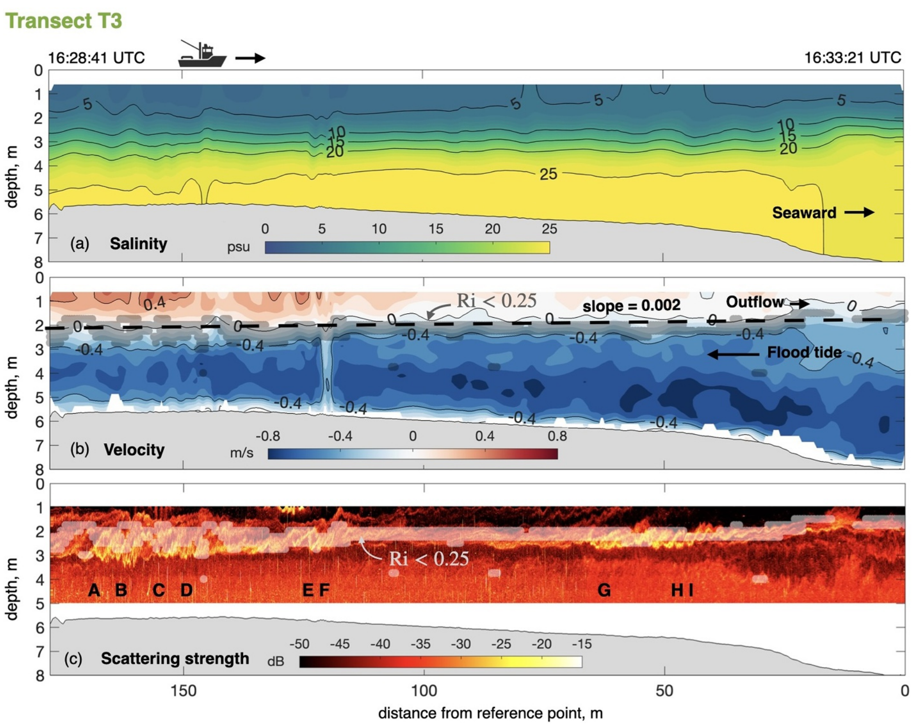

Figure 6. Overview of transect T3, starting 2 hr 23 min after slack water. Track direction is left to right (seaward). Same legend as Figure 4. Multibeam images are shown at locations A, B, …, I in Figure 9.

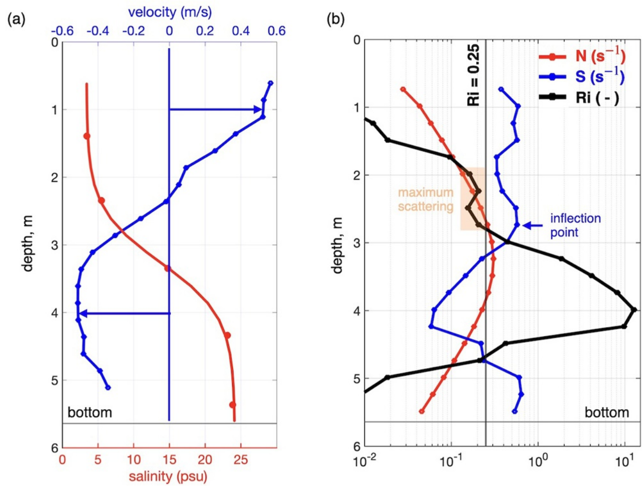

Figure 7. Typical profiles, here taken from transect T2. (a) Salinity (in red) at along-transect distance 75 m (see Figure 5). Note the five CTD sensors and the hyperbolic-tangent fit applied to all salinity data. The velocity profile from the acoustic Doppler current profiler was averaged over the window $70-80$ m. (b) Buoyancy frequency N (red), shear S (blue) and Ri (black). Maximum scattering from mixing in Figure 5 occurs where Ri < 0.25 and $N > 0.15\ \mathrm{s}^{-1}$ (highlighted in orange).

simple rule of thumb for the KH growth rate is $\approx S\left(1/4-\min_z \mathrm{Ri}\right)^{1/2} < S/2$ (Hazel, 1972), which here gives an upper bound of $0.4\ \mathrm{s}^{-1}$. These fast N and S timescales underscore why such shallow-wedge estuaries are well suited to the acoustic imaging of mixing: shallow depth and sharp salinity contrasts enhance the multibeam data resolution and signal-to-noise ratio, while intrinsic shear times of order one second allow instability trains to be tracked over just a few minutes.

Figure 8b shows the corresponding distribution of Ri (light gray histogram), with particular emphasis on the minimum values across the 2–4 m depth range (dark gray histogram). While the entire distribution peaks just below 0.25, consistent with prior measurements in this estuary (Geyer et al., 2017), the $\min_z$ Ri distribution lies almost entirely below 0.25, is approximately normal, and peaks around Ri $\approx 0.10-0.15$. This peak sits well below the linear stability threshold 0.25 (Equation 1), often cited in the literature on marginal instability as the value around which turbulence self-organizes, as found, for example, in the Pacific and Atlantic equatorial undercurrents (Smyth, 2020; Smyth & Moum, 2013; Wenegrat & McPhaden, 2015) and within internal solitary waves (Chang, 2021). We interpret our submarginal Ri as evidence that turbulence in this estuary is strongly forced by the tide and the sloping pycnocline.

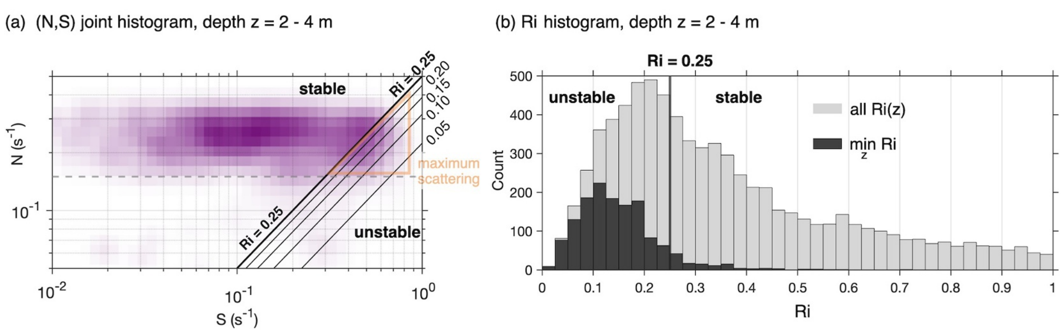

Figure 8. Typical N, S and Ri in all transects T1, T2, T3 between depths $2-4$ m. (a) Joint histogram (S, N) with purple shading intensity proportional to probability density. The region of typical maximum scattering is highlighted. (b) Histogram of Ri (gray) with emphasis (black) on the distribution of the minimum Ri in each profile between $2-4$ m, showing a peak just below Ri $= 0.15$, well below the marginal instability value of 0.25. The long tail of stable Ri > 1 is not shown.

3.2. Large-Scale Baroclinic Forcing and Dissipation

This forcing can be modeled as follows. The primary (large-scale) slope of the pycnocline was estimated in transects T1–T3 to be $\alpha \approx 0.002$ (Figures 4–6). Since the large-scale pressure gradient must remain nearly vertical (hydrostatic), the misaligned buoyancy gradient generates a baroclinic torque that energizes the shear at a rate

$$\frac{dS}{dt} \approx \alpha N^2, \tag{6}$$

where $\alpha \ll 1$ denotes the (dimensionless) slope. In this paper, "baroclinic" refers to the classical fluid-dynamical mechanism whereby the misalignment of pressure and density gradients generates vorticity (Vallis, 2017, see Equations 4.16–4.17). Under this baroclinic forcing, an initially stable water column with $\min_z \mathrm{Ri}(t=0) = \mathrm{Ri}_0 = N_0^2/S_0^2 > 0.25$ (say 0.3) will experience a steady decrease of this Richardson number following $\min_z \mathrm{Ri}(t) = \mathrm{Ri}_0/(1 + 2\alpha\,\mathrm{Ri}_0\,S_0 t)$. In other words, the timescale for halving the initial Ri from, say, 0.3 to 0.15 under this forcing is $(2\alpha\,\mathrm{Ri}_0\,S_0)^{-1}$; in our case $\approx (2 \times 0.002 \times 0.3 \times 0.5)^{-1} \approx 27$ min. This is much shorter than the tidal period, consistent with our argument that baroclinic forcing is the primary mechanism driving the flow to a state of submarginal instability within a single tidal phase. In our shallow estuary, baroclinic shear arises from the time-dependent response of the pycnocline to tidal forcing in the presence of bathymetric slopes. In transect T0, the primary slope of the pycnocline supporting the KH billow train matches the bathymetric slope $\alpha = 0.02$ (see Figures 1a and 1c), which is an order of magnitude steeper than in T1–3 and implies a forcing timescale for Ri about 10 times faster, of order 3 min.

The baroclinically-forced decrease in Ri will eventually be arrested once turbulence becomes strong enough, at an equilibrium value $\mathrm{Ri} \approx 0.1$–0.15. This value must be sufficiently below 0.25 to generate strong enough Reynolds stresses $\overline{u'w'}$ and associated energy dissipation ϵ to balance the forcing αN^2 and establish a turbulent steady state for the shear:

$$\frac{\partial S}{\partial t} \approx \alpha N^2 - \left|\frac{\partial^2}{\partial z^2}\overline{u'w'}\right| \approx 0. \tag{7}$$

Solving for the Reynolds stresses across the shear layer $z \in [0, \delta]$, we find $\overline{u'w'} \approx \alpha N^2 z(z-\delta) \propto \alpha N^2 \delta^2$. The corresponding dissipation within the large-scale turbulent pycnocline largely follows the shear production (the buoyancy flux is small, since mixing efficiency is typically $\Gamma \ll 1$) and must therefore scale like

$$\epsilon \propto P = |\overline{u'w'}|S \propto \alpha\,N^2\,S\,\delta^2 \propto \alpha\,\mathrm{Ri}\,S^3\,\delta^2, \tag{8}$$

where $\Delta U = S\,\delta$ is the total velocity differential across the shear layer.

In Section 5.2, we return to this balance to quantify small-scale dissipation within the braids, which is likewise driven by baroclinic-slope forcing. The last equality in Equation 8 includes a pre-factor of 0.05, as shown later in Equation 15. Using this prefactor, we estimate a large-scale average in T1–3 of $\epsilon \approx 10^{-5}\ \mathrm{m^2\,s^{-3}}$ (using $\alpha = 0.002$ from Figures 4–6 and $S = 0.5\ \mathrm{s^{-1}}$, $\delta = 2$ m from Figure 7), noting that α and thus ϵ are an order of magnitude higher in T0 (Figure 1). This value is well above expected background dissipation levels in a quiescent estuarine pycnocline and is consistent with previous measurements in the same estuary (Lavery et al., 2013, Figure 8a). However, those measurements, as well as others (Holleman et al., 2016, Figure 7a), also revealed highly localized peaks at $\epsilon \sim 10^{-3}\ \mathrm{m^2\,s^{-3}}$, implying that the pycnocline average masks much smaller and more intensely dissipative structures—the focus of this paper.

3.3. Turbulent Length Scales and Multiscale Approach

We end this section by outlining the expected hierarchy of length scales in the turbulent cascade of our estuarine data. The challenge arises from the very high Reynolds number Re and Schmidt number Sc (defined as the ratio of ν to the molecular diffusivity of salt D). In transects T1–3, we find that

$$\mathrm{Re} = \frac{(\Delta U/2)(\delta/2)}{\nu} \approx 7.1\text{–}8.8 \times 10^5 \quad \text{and} \quad \mathrm{Sc} = \frac{\nu}{D} \approx 600\text{–}1000 \tag{9}$$

For the range of Re, we used the transect-averaged velocity profiles, half the total velocity differential ΔU and half the shear layer depth δ for consistency with much of the literature of stratified shear instabilities. We also used an averaged $\nu = 1.05 \times 10^{-6}$ $\mathrm{m^2\ s^{-1}}$. For the range of Sc, we used the salinity-dependent values of ν and D for sodium and chloride ions in the mixing range 5–20 psu, at the average temperature of 20°C. To fix ideas, here and in the remainder of the paper, we shall use the following representative values

$$\mathrm{Ri} = 0.15, \qquad \mathrm{Re} = 8 \times 10^5, \qquad \mathrm{Sc} = 700. \tag{10}$$

We also recall our large-scale estimate $\epsilon \sim 10^{-5}\text{–}10^{-4}\ \mathrm{m^2\ s^{-3}}$, supported both by the baroclinic-slope forcing scaling and previous measurements in this estuary, and that maximum scattering (mixing) occurs at $N \sim 0.15\text{–}0.2 \sim 10^{-0.75}\ \mathrm{s^{-1}}$. Using these values, we estimate the three key length scales—the Ozmidov scale L_O, the Kolmogorov scale L_K and the Batchelor scale L_B—as

$$L_O = \left(\frac{\epsilon}{N^3}\right)^{1/2} \approx 2\text{–}6\,\mathrm{cm}, \quad L_K = \left(\frac{\nu^3}{\epsilon}\right)^{1/4} \approx 0.4\text{–}0.6\,\mathrm{mm}, \quad L_B = \frac{L_K}{\mathrm{Sc}^{1/2}} \approx 13\text{–}25\,\mu\mathrm{m}. \tag{11}$$

The Ozmidov scale can be interpreted as the largest horizontal scale with sufficient kinetic energy to overturn (Riley & Lindborg, 2008). At scales smaller than L_O, buoyancy effects are dynamically weak and turbulence behaves increasingly like weakly stratified small-scale turbulence, though not strictly isotropic (Gargett et al., 1984; Portwood et al., 2019). In this range we expect a $k^{-5/3}$ inertial subrange in the kinetic energy and scalar variance spectra, extending down to a few L_K. At smaller scales, velocity fluctuations are exponentially damped, but scalar (salinity) fluctuations persist because of the high Sc. In this viscous–convective subrange the scalar variance spectrum likely follows a k^{-1} scaling down to a few L_B (Kundu et al., 2016, Chap. 12), where resolving structures typically remains beyond present observational, experimental and numerical capabilities at such high Sc.

The separation between L_O and L_K quantifies the width of the inertial subrange. Through the equality $L_O/L_K = \mathrm{Re_b}^{3/4}$, it connects to the buoyancy Reynolds number $\mathrm{Re_b}$—a key parameter of stratified turbulence—which we estimate as

$$\mathrm{Re_b} = \frac{\epsilon}{\nu N^2} \approx 300\text{–}3{,}000 \tag{12}$$

Prior studies argued that a dynamic range of $\mathrm{Re_b} \gtrsim 30$ is necessary for the existence of an inertial subrange, and thus, of stratified turbulence (Bartello & Tobias, 2013), and that $\mathrm{Re_b} \gtrsim 300$ is necessary to small-scale isotropy (Portwood et al., 2019). The above range of large-scale $\mathrm{Re_b}$ in the main pycnocline thus indicates strongly energetic stratified turbulence. It is consistent with prior measurements in this estuary (Holleman et al., 2016, Figure 10), though toward the lower end, again suggesting that smaller-scale peak ϵ values may be dynamically more relevant than large-scale transect averages. Comparable $\mathrm{Re_b}$ values have been reported in other strongly stratified estuaries (Geyer et al., 2008), and more broadly, in a range of other forced environments like mid-ocean ridges, the equatorial undercurrent, Arctic fjords, lake hypolimnia, the main thermocline, and the upper oceanic mixed layer (Jackson & Rehmann, 2014, Figure 14). This similarity in $\mathrm{Re_b}$ underscores the broad relevance of these estuarine observations for ocean mixing.

To bridge the hierarchy of turbulent mixing processes, we combine (a) ADCP/CTD data defining the large-scale hydrodynamic and energetic context at the meter scale, (b) detailed acoustic observations resolving anisotropic braid structures down to cm scale, near the Ozmidov limit, and (c) numerical simulations and laboratory experiments extending the picture to the sub-mm Kolmogorov scale.

4. Detailed Acoustic Observations

4.1. Multibeam Visualizations of Shear Instabilities at Peak Amplitude

We now turn to instantaneous multibeam visualizations of the shear instabilities that mix the main pycnocline. Figure 9 presents 30 snapshots from transects T1–T3 at the locations labeled A, B, C, … in Figures 4–6c. The multibeam aperture, together with the shallow depth (1–5 m), provides an 8 m horizontal window, typically spanning a single instability wavelength. As the vessel progresses along the transect (see supplementary movies in Lefauve et al. (2026)), individual instability "events" between $2-4$ m depth enter and exit this window while evolving under their own dynamics, including: (a) growth, seen in the movies as steepening of the bright yellow high-χ_s structures; (b) decay, as the structures flatten; (c) right-to-left propagation, caused by the typical landward velocity at the velocity inflection point; and (d) highly-nonlinear distortion, including merging and splitting of wavelengths, and occasional interference with instabilities nearer the surface (examples of these temporal evolutions are shown in the next section). These 30 snapshots capture all distinct instability events in T1–T3 at maximum slope (peak amplitude).

Three important observations emerge from these visualizations. First, there is little, if any, evidence of "bright cores," that is instabilities overturning at the scale of the primary KH billow (typically ∼1 m tall). Instead, intense turbulent mixing χ_s is concentrated along "bright braids" and other thin, elongated structures between the primary "quiet cores." Single-beam observations and finescale measurements had previously suggested this pattern (Geyer et al., 2010; Vladoiu et al., 2025), but multibeam imagery confirms it and shows it is generic across a large sample of events spanning three transects.

Second, the bright turbulent braids exhibit shallow slopes, on the order of $\alpha \approx 0.1–0.5$ (see white guide lines in the bottom right of each panel). Figure 10 provides the histogram of slopes measured by fitting a line through the steepest, physically meaningful braid in each of the 30 snapshots. The distribution is approximately bell-shaped around the mean slope $\alpha \approx 0.25-0.35$. This observation is novel in that multibeam imagery provides reliable slopes, and it is significant in showing that, even at maximum amplitude, the instabilities do not steepen sufficiently (to, say, $\alpha \sim 1$) for billows to overturn and drive mixing directly. This stands in contrast to numerical simulations and laboratory experiments at comparable $\mathrm{Ri} = 0.1-0.15$ but lower $\mathrm{Re} \sim 10^3–10^4$ (see references in the introduction), where instabilities steepen further and cause the primary billow to overturn and mix.

Third, the bright braids occasionally display small-scale granularity, most clearly in panel T2E, suggesting discrete turbulent billow cores on the braid scale (∼10 cm). Later in this paper we argue that these features result from secondary KH instability on the braid itself. The relative rarity of such clear, discrete braid billows in Figure 9 may be explained by two factors: (a) the acoustic data can only resolve structures larger than ∼5 cm, comparable to the braid billow height, so small individual billows may be smoothed into what appears as a continuous bright braid; (b) this overturning billow stage may be inherently short-lived, followed by a much longer incoherent turbulent-braid phase, seen in most other snapshots.

The added value of multibeam imagery compared with single-beam is illustrated in Figure 11. We compare a selection of six of our multibeam snapshots (e.g., T1E, etc.) with their corresponding synthetic middle-beam reconstructions (labeled T1E (R), etc.). These reconstructions mimic what a single-beam echosounder, such as in the AUV data of Figure 1, would record. These six examples differ in the time required for the vessel to sweep the 8 m window, depending on local vessel speed. Sweep time, noted above each panel, increases from left to right and top to bottom, making single-beam reconstructions progressively more prone to Doppler distortion as the instabilities evolve and move with finite phase speed while being scanned by the sonar. Faithful single-beam reconstructions would require sweep speeds much faster than the instability phase speed (here $\sim 0.1–0.2$ m s^{-1}), which is difficult to achieve in practice. Sweep direction, determined by the heading of the measurement platform, also matters: when the vessel moves with the instability (landward in T1), structures appear stretched and slopes flattened, whereas sweeps against the propagation direction (T2, T3) compress structures and steepen slopes. In both cases, distortion increases as sweep speed approaches wave speed. Accordingly, the most faithful single-beam reconstruction is found in T1E (top left), where the fast sweep speed ≈ 2 m s^{-1} and favorable direction yield the closest match to the multibeam. Single-beam images degrade progressively with slower sweep speeds and unfavorable vessel headings, becoming unrecognizable and misleading in T2F and T2N (sweep speeds $\approx 0.2–0.3$ m s^{-1}). Thus KH wavelengths and billow aspect ratios inferred from single-beam acoustics in past studies (see e.g., Tu et al., 2020, Table 1) should be treated with caution.

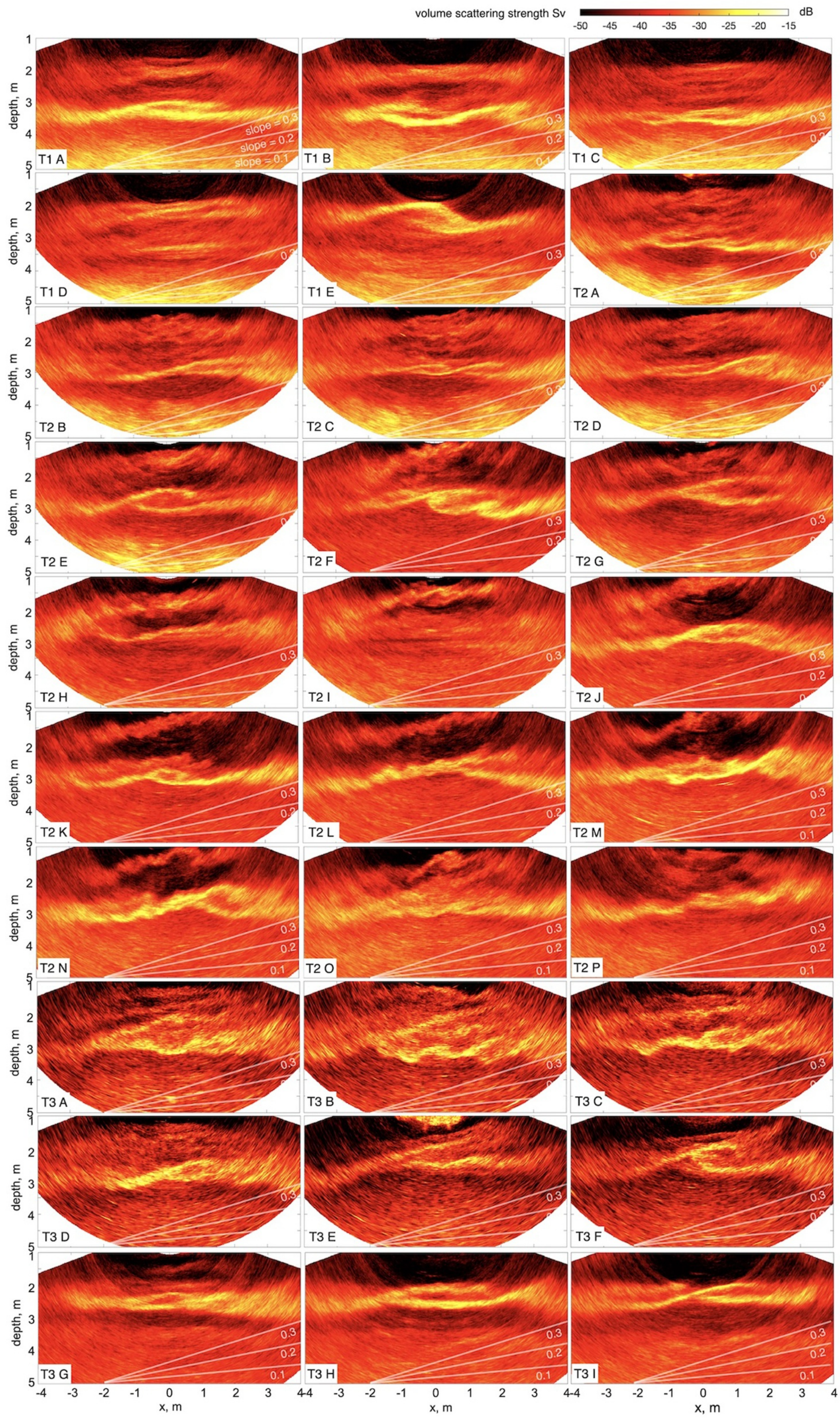

Figure 9. Multibeam imagery of shear instabilities in 30 separate events selected at maximum braid slope. Snapshot lettering is as per Figures 4–6c, e.g. "T1 A" refers to transect 1 at location "A", etc. Right is seaward, so flow in the bottom layer (depth $\gtrsim 3$ m) is always right to left (flood tide), and vice versa in the surface layer.

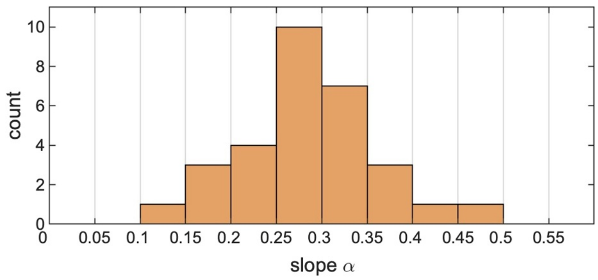

Figure 10. Histogram of braid slopes α estimated in the 30 representative multibeam snapshots of Figure 9. The minimum and maximum observed values are 0.14 and 0.46, respectively.

4.2. Spatial Evolution of the Primary KH Train

Using these insights, we reassess the single-beam T0 data from Figure 1c, reproducing it enlarged in Figure 12 with a 1:1 aspect ratio. Given the AUV's relatively fast sweep speed (1 m s^{-1}) and the favorable sweep direction (landward during flood tide), the structures in Figure 12 are likely sufficiently faithful to provide supporting evidence to the multibeam observations from the previous section. We follow the spatial development of the primary instability over 73 m (panel a), with three 22 m sections enlarged in panels b–d, covering 11 separate wavelengths labeled #1–11 (average wavelength ≈5.5 m). Note that the spatial evolution and wavelength number run from right to left and bottom to top.

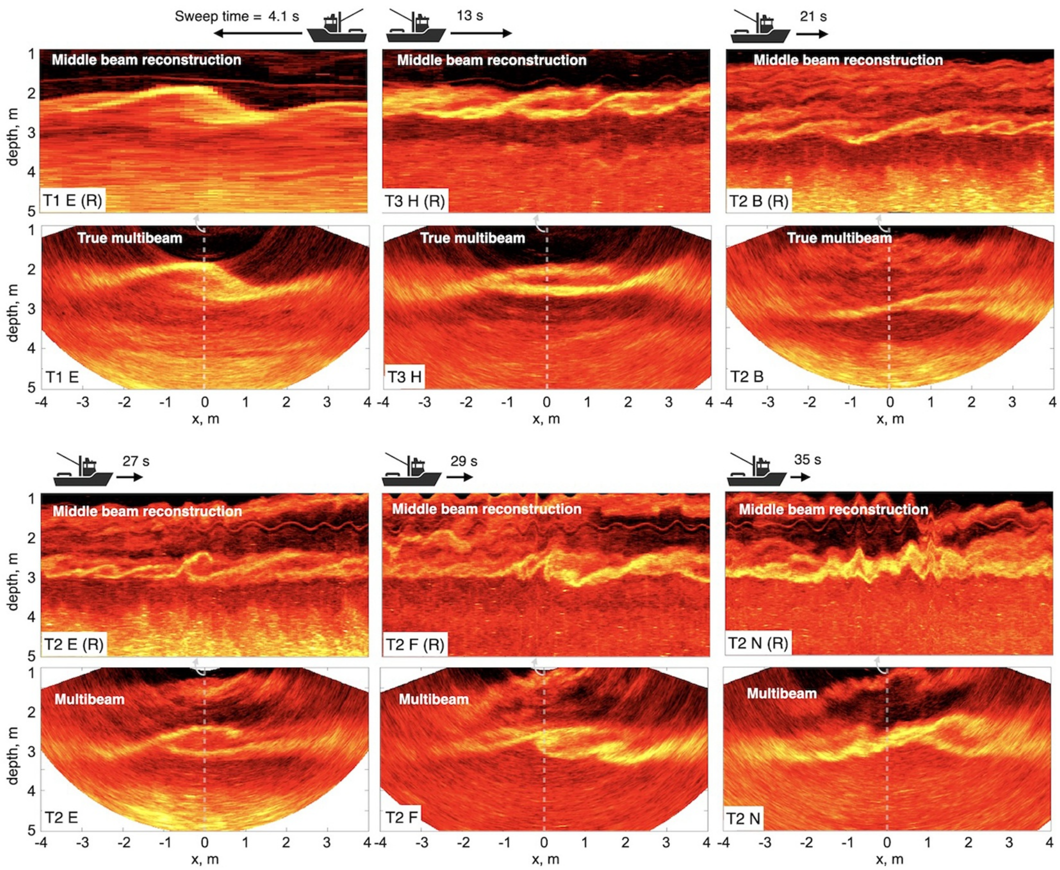

Figure 11. Multibeam imagery preserves mixing structures, as demonstrated by contrast with middle-beam reconstructions, labeled (R), using the $x = 0$ beam. Multibeam snapshots are repeated from Figure 9. Vessel sweep time increases from left to right and top to bottom, making single-beam imagery increasingly prone to distortion and thus unreliable to infer structures. Color range identical to Figure 9.

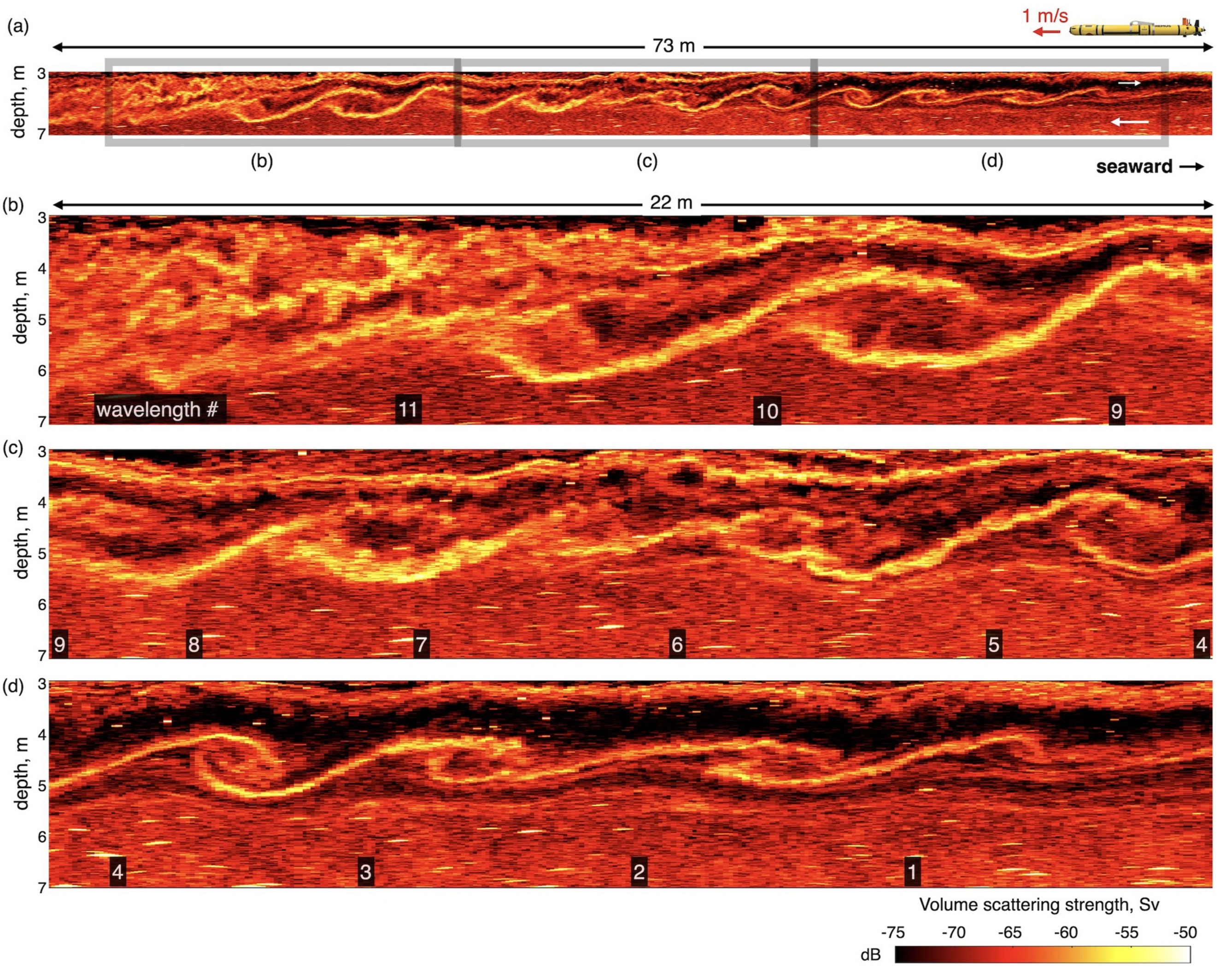

Figure 12. Zoom on the T0 data from Figure 1, without vertical exaggeration (1:1 aspect ratio), highlighting secondary instabilities within the braids. The long section from (a) is split into three 22 m-long enlarged sections in (b)–(d). Individual wavelengths are numbered 1–11 in chronological order (the autonomous underwater vehicle sweep direction is landward, right to left). As with any single-beam data, structures and slopes remain uncertain but are reasonably accurate here due to the fast sweep speed and favorable heading.

In the early stages of instability (#1–2, panel d), we find thin braids (thickness ≈1–3 cm) and moderate slopes, gradually steepening in #3–4. Notably, a partial overturn of a primary KH billow occurs between #3–4—a rare event, consistent with our earlier observations. Nevertheless, even in this case of partial overturn, mixing remains concentrated in the bright “eyelids”, extensions of the braid that wrap around the core or “eye”, rather than within the cores themselves, ruling out mixing caused by gravitational collapse of the 1 m-tall core.

At intermediate and later stages (#4–10, panels c and b), braids continue to steepen without primary overturn. Some braids develop marked granularity, particularly evident in #5, confirming the presence of secondary instabilities. The more mature braids (#9–10) are thicker (≈10 cm) and slightly brighter, indicating that turbulence and mixing have intensified and spread across the braid, likely triggered by the earlier secondary instabilities and sustained by the baroclinic slopes of the braids.

At the later stages of the instability (#11 and leftwards, panel b), further downstream of the mean landward flow, the braid loses coherence and breaks down into more disorganized turbulence. This turbulence, however, remains roughly aligned with the former braid slope (and underlying isopycnals) and continues to sustain high levels of mixing.

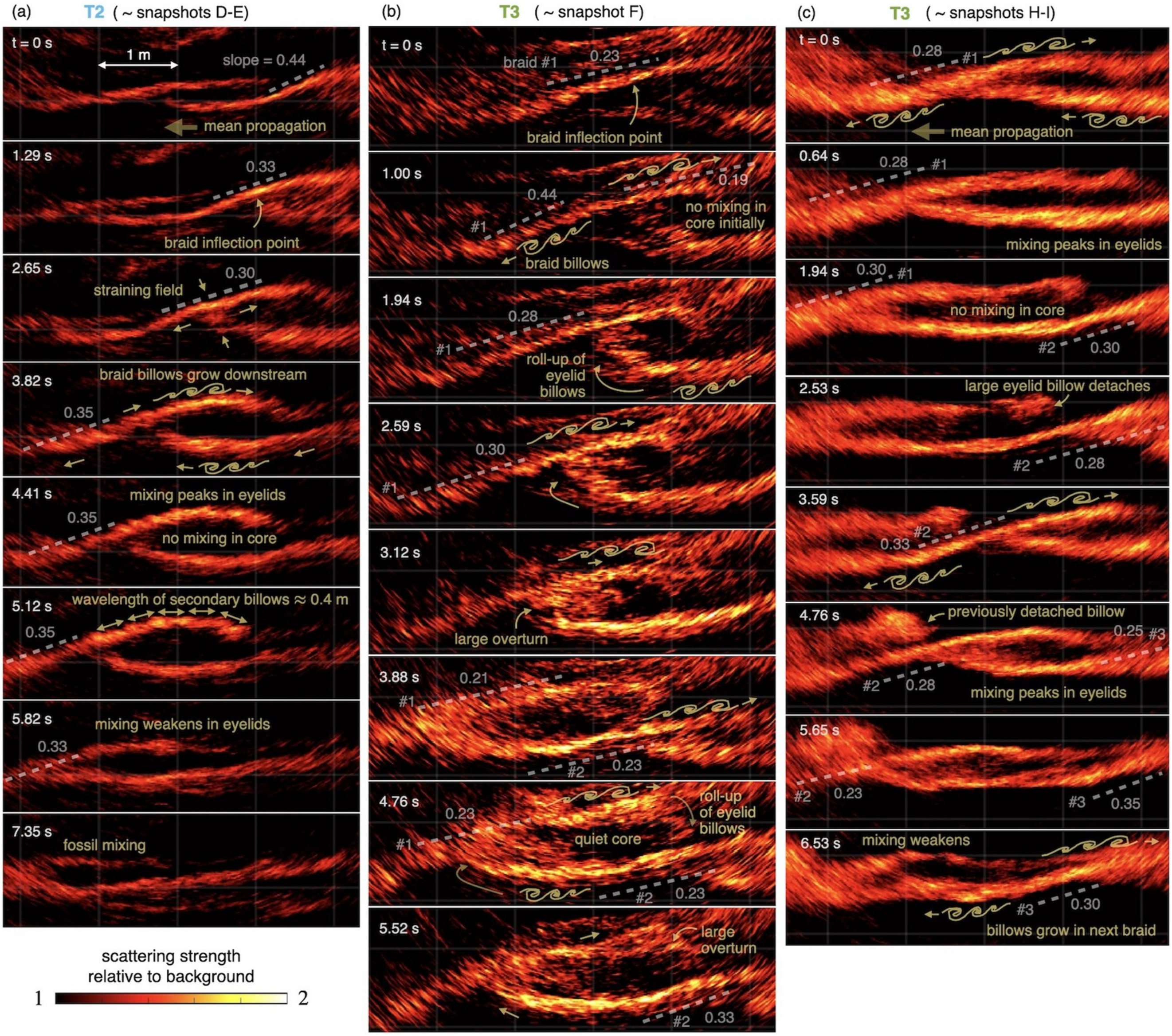

Figure 13. Temporal evolution of individual shear instabilities revealed by three multibeam sequences from transects T2 and T3 to illustrate their typical lifecycle. Each column shows one or two events around the maximum-amplitude snapshots from Figure 9, extended in time to capture growth, overturn, and decay. Time increases downwards. Gray annotations help track braid numbers # across frames and quantify slopes. Yellow annotations condense dynamical information from the movies. The scattering strength is normalized by the transect-mean background. The light-gray grid has 1 m spacing.

4.3. Multibeam Visualization of the Lifecycle of Mixing

We now seek to better understand the complex lifecycle of these instability structures, one wavelength at a time, by returning to time-resolved multibeam imagery. In Figures 13 and 14 we show six sequences of snapshots from transects T2 and T3, with elapsed time indicated on the left. Each column follows an event in the vicinity of the snapshots shown earlier at maximum amplitude (e.g., T2D and T2E in Figure 13a etc.), now extended in time to reveal their growth and decay. Unlike previous visualizations, here the scattering strength is normalized by the transect-mean background ($|S_V(x,z,t|)/|\overline{S_V}(x,z)|$) to enhance contrast and highlight regions of elevated $\log_{10}\chi_s$ relative to the substantial background in this environment. Gray overlaid annotations indicate the slopes of the most meaningful braids and wavelength numbers # to track events as they propagate and distort across frames.

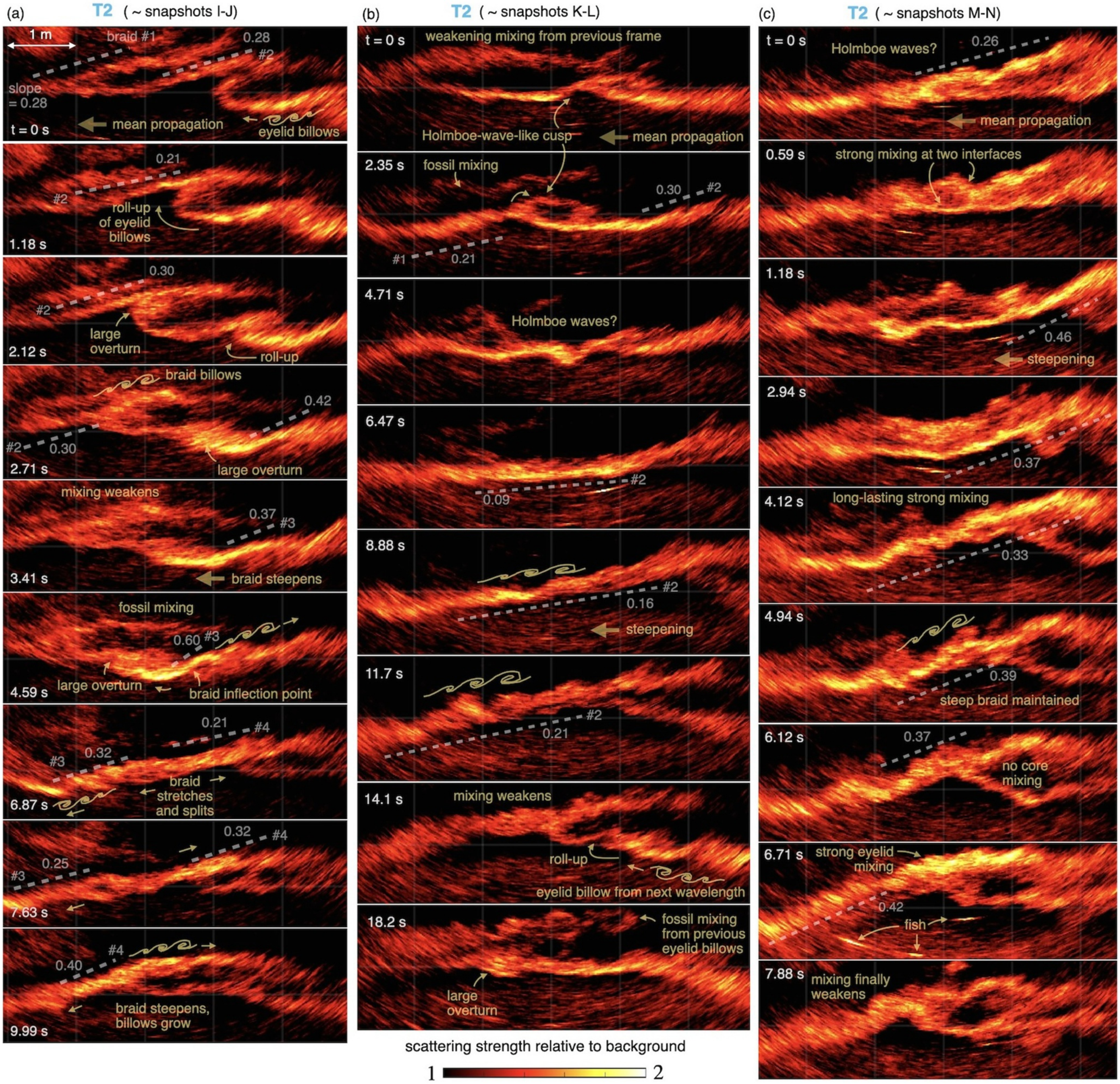

Figure 14. Temporal evolution of individual shear instabilities shown in three further multibeam sequences from transect T2 to illustrate more complex lifecycles. Legend as in Figure 13.

Additional yellow annotations highlight key dynamical features identified after careful inspection of the 17 Hz movies, condensing a large amount of information.

The first sequence in Figure 13a shows an initially steep braid ($\alpha = 0.44$ at $t = 0$) propagating leftward (landward) over several seconds, maintaining a nearly constant slope ($\alpha \approx 0.35$). Braid mixing initially peaks at the inflection point ($t = 1.29$ and 2.65 s), where the local straining field arises from deflection of the mean shear around the meter-tall billows on either side. A few seconds later ($t = 3.82$ and 4.41 s), mixing intensifies further downstream in a train of smaller-scale billows that grow spatially along the braid and into the eyelids, under advection on either side of the inflection point ($t = 5.12$ s). These small turbulent eyelid billows, with wavelength $\approx$0.4 m, eventually concentrate most of the mixing in the pycnocline. Less than a second later ($t = 5.82$ s), eyelid mixing weakens rapidly, leaving only "fossil" mixing ($t = 7.35$ s). Throughout this event, the primary core remains dark, indicating no mixing above background levels and confirming that it does not overturn. This sequence reveals a timescale of about 5 s for sustained braid and eyelid turbulence, followed by decay over ≈2 s. Assuming similarity between primary and secondary KH instabilities, the observed secondary billow wavelength (≈0.4 m) implies a braid thickness $\delta \approx$ 10–15 cm at the mature stage, consistent with our previous estimates.

The second sequence in Figure 13b begins with a relatively weak braid #1 ($\alpha = 0.23$) that steepens rapidly to $\alpha \approx 0.44$. Mixing is initially absent in the core, appearing instead in the braid and eyelid billows. Between $t = 1.94$ s and $t = 3.12$ s a large overturn develops through the roll-up of the bottom eyelid billows, yet the core remains dark. In the later frames ($t = 3.88$–5.52 s), the top eyelid experiences a similar fate, with roll-up to the right of the core, which remains shielded. The next braid #2, coming from the right, starts steepening (from $\alpha = 0.23$ to 0.33), signaling the start of the next event. This sequence confirms that even strong steepening to $\alpha \approx$ 0.4–0.5 does not trigger core mixing by large-scale gravitational collapse. Rather, turbulence grows and peaks in the braids and eyelids, and may occasionally be engulfed into the core—though this did not occur in the first sequence.

The third sequence in Figure 13c shows three successive wavelengths (#1–3) propagating landward faster than in the previous sequences. All three follow a similar lifecycle to that described in Figure 13a, giving robustness to our interpretation. A minor novelty appears at $t = 2.53$ s when a large eyelid billow from #1 detaches, and is advected in the vicinity of the neighboring braid #2 in subsequent frames ($t = 3.59$–4.76 s) before weakening ($t = 6.53$ s).

We now turn to Figure 14 to illustrate some of the additional complexity in the lifecycles. The fourth sequence (Figure 14a) begins with a fairly standard roll-up of braid billows into the core. From $t = 3.41$ s, however, braid #3 steepens dramatically and then stretches and splits ($t = 6.87$ s), likely under intense strain. The splitting generates braid #4, which then follows the more typical lifecycle.

The fifth sequence (Figure 14b) begins with the familiar pattern of fossilizing eyelids, but gradually transforms into what appears to be a Holmboe instability ($t = 0-4.71$ s), recognizable by the characteristic cusps (Carpenter, Tedford, et al., 2010) in the turbulent pycnocline. The Holmboe instability is a strongly-stratified cousin of the KH instability that arises when the pycnocline is much thinner than the surrounding shear layer (Caulfield, 1994). Such features may reflect mixed KH–Holmboe instability modes when the shear and density gradients are vertically offset (Carpenter, Balmforth, & Lawrence, 2010; Tedford et al., 2009). In the present case this may represent a temporary state, after the mean shear has been weakened by a turbulent event and before it is re-energized by the baroclinic-slope forcing. Soon after, the pycnocline ($t = 6.47$ s) steepens again ($t = 8.88$ s) as the primary KH instability redevelops following the typical lifecycle.

The sixth and last sequence (Figure 14c) starts with Holmboe-like cusps revealing strong mixing at two interfaces ($t = 0.59-2.94$ s), with a braid that transiently steepens to a rarely seen $\alpha = 0.46$. It then flattens to more typical $\alpha = 0.3-0.4$ and sustains intense mixing for a typical ≈5 s, with signs of stretching and splitting, while the core remains dark throughout. Eyelid mixing peaks and thickens ($t = 6.71$ s) before suddenly weakening ($t = 7.88$ s). These six sequences are available as supplementary movies in Lefauve et al. (2026).

The observations in this section show that, in the continuously forced regime, the lifecycle of shear instabilities only lasts a few shear timescales, which is at least an order of magnitude faster than that of the idealized KH instabilities typically simulated. These observations also raise at least three questions that we turn to next with modeling. Why do braids consistently develop secondary small-scale billows where mixing concentrates, and what are the relevant local length- and time scales? How is turbulence in the braids and eyelids generated and sustained, and what levels of ϵ and χ_s should we expect at the braid (Ozmidov) scale of ~10 cm? What does mixing look like well below the braid scale, down to the Kolmogorov scale? The complementary numerical and laboratory approaches presented next are not intended as direct reproductions of unresolved field-scale turbulence, but rather as physically consistent frameworks for interpretation.

5. Modeling and Discussion

5.1. Secondary KH Instabilities Predicted From Numerical Simulations

To understand why secondary billows consistently appear along the braids while cores remain quiet, we conducted 2D DNS at field conditions. The flow was initialized with hyperbolic-tangent velocity and salinity profiles

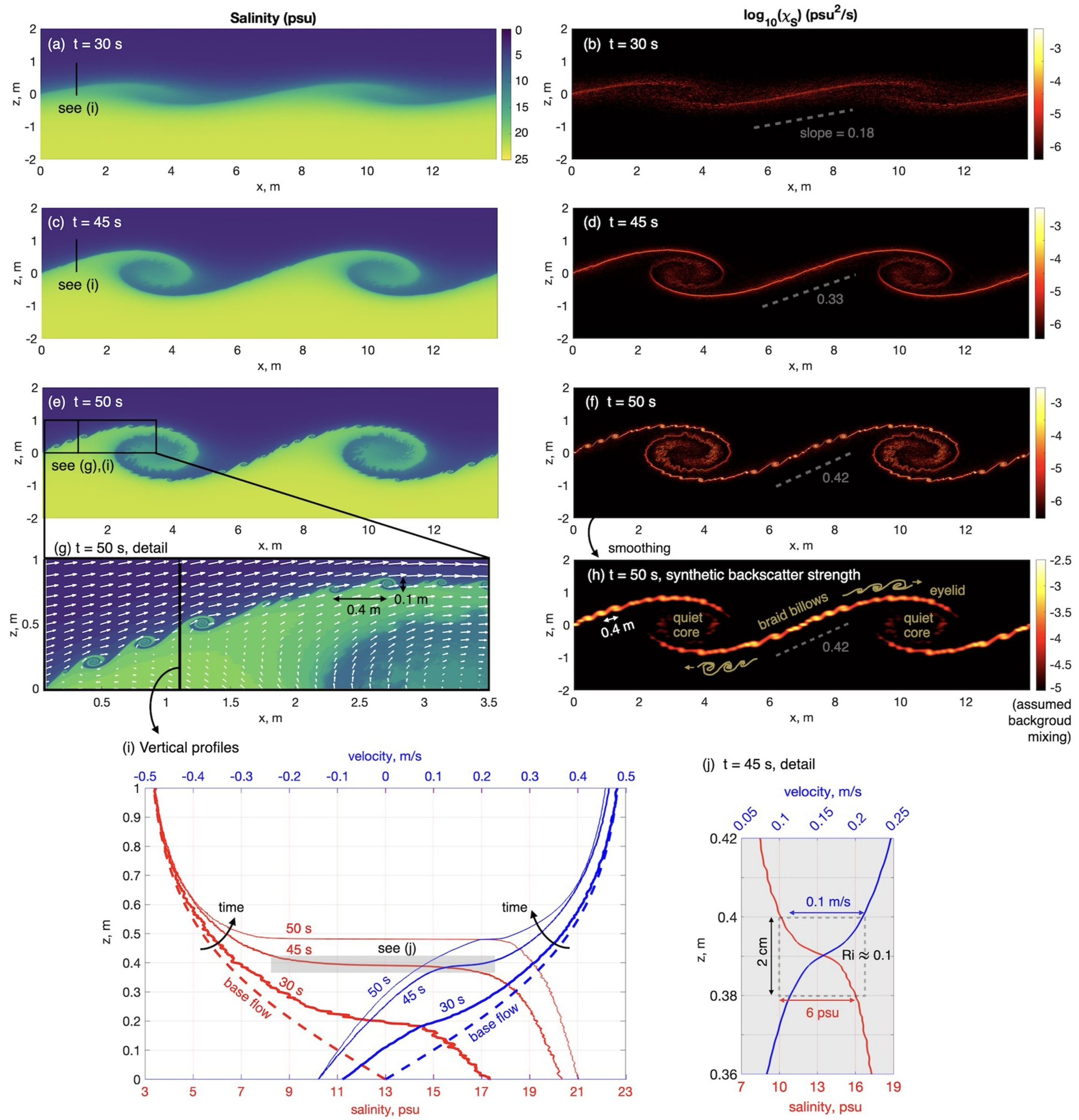

Figure 15. Two-dimensional direct numerical simulation revealing secondary KH instability on the braid at field-matched (Ri, Re, Sc). (a, c, e) Salinity and (b, d, f) its mixing rate $\log_{10}\chi_s$ at $t = 30, 45, 50$ s after initialization. (g) Zoom on the salinity with velocity vectors, showing the braid after onset of secondary instability. (h) Synthetic backscatter obtained by Gaussian smoothing and colormap clipping so that values below the expected background $\chi_s < 10^{-5}$ psu^2 s^{-1} appear as baseline (black) for comparison with Figures 13 and 14. Two wavelengths are shown for clarity, and the domain has been cropped to $z \in [-2, 2]$ m. (i) Vertical profiles across the braid, showing extreme sharpening over time. (j) Detail over a 6-cm window within the braid at onset of secondary instability.

consistent with the typical profiles in Figure 7, with dimensionless parameters set to our representative field values $(\mathrm{Ri}, \mathrm{Re}, \mathrm{Sc}) = (0.15, 8 \times 10^5, 700)$ (see Equation 10). The Navier–Stokes equations under the Boussinesq approximation were solved with `Oceananigans.jl` (Ramadhan et al., 2020) with very fine resolution

(12,000 × 12,000 grid points) to capture braid sharpening. Details of the numerical setup (grid, initial and boundary conditions) are given in Appendix C.

Figures 15a–15f illustrate the evolution of the primary KH braid (a supplementary movie is available at Lefauve et al. (2026)). At $t = 30$ s it has slope $\alpha \approx 0.2$ (panels a–b); by $t = 45$ s it steepens to $\alpha \approx 0.3$ and shows signs of instability (panels c–d), and by $t = 50$ s it has developed secondary KH billows at $\alpha \approx 0.4$ (panels e–f). The dynamics are expected to remain essentially 2D until soon after $t = 45$ s. By $t = 50$ s, the secondary billows have already overturned multiple times (see zoom in panel g), implying that in three dimensions they would have already transitioned to turbulence, while the braid slope remains fairly shallow and before the primary billows overturn significantly. Thus, these simulations confirm that, at these field-matched parameters, vigorous turbulence on the braid is expected to precede primary core turbulence.

The simulation agrees closely with our observations on three points, strengthening our confidence in their relevance. First, the secondary billow spacing (~ 0.4 m) and height (~ 0.1 m) shown in panel g match the multibeam imagery. Once turbulent, the braid may thicken slightly by entrainment, consistent with our earlier estimate $\delta \approx 0.1 - 0.15$ m at the mature stage. Second, simulated braid slopes (panels b,d,e) fall in the observed range $\alpha = 0.2 - 0.4$ (Figure 10) and confirm that braid turbulence sets in below or around $\alpha \approx 0.4$. Steeper slopes, which would favor primary overturn, are rare in the field presumably because braid turbulent dissipation intervenes first and arrests primary growth. Third, the simulated mixing structure ($\log_{10} \chi_s$) is consistent with the multibeam echosounder signal. To illustrate this, panel (h) shows a synthetic backscatter obtained by Gaussian smoothing and colormap clipping below $\chi_s < 10^{-5}$ psu^2 s^{-1}, mimicking sonar acquisition and emphasizing only mixing above pycnocline background levels. The result strongly resembles Figure 13a around peak mixing ($t = 4.41$ s).

What mechanism drives this secondary instability? As the braid steepens, it experiences a compressive strain field from the deflection of the mean shear flow around the growing billows (see velocity vectors in panel g). This strain $\gamma = |\partial w/\partial z|$ is initially sufficient to stabilize the braid (Corcos & Sherman, 1976; Dritschel et al., 1991; Smyth, 2003; Staquet, 1995). As the braid slope α increases, baroclinic forcing amplifies the shear at a rate $dS/dt \approx \alpha N^2$ (recall Equation 6), while strain compresses the isopycnals and increases the local N^2, sharpening both the pycnocline and the shear layer, as seen in the vertical profiles in panel (i). At high Re, diffusion is too small to smooth these gradients, allowing local shear to intensify much more rapidly than strain, whose growth remains moderate and controlled by the large-scale primary billow. Previous studies suggest that once S/γ exceeds a threshold, the braid succumbs to secondary KH instability (Mashayek & Peltier, 2012a; Smyth, 2003; Staquet, 1995). When the secondary billows saturate—here around $t = 50$ s—the effective braid thickness (secondary billow height) is ~ 0.1 m, but the velocity and salinity profiles are no longer hyperbolic–tangent, that is similar to the larger scale. A fine zoom on the braid (panel j) shows that, within it, even from $t = 45$ s, the sharpest gradients are confined to an even thinner ~ 2 cm interface (dashed box). This intense local sharpening is consistent with prior high-resolution CTD measurements in this estuary revealing ~ 1 cm-sharp pycnoclines (Figure 6b in Holleman et al. (2016)). Within the 2 cm interface in Figure 15j, Ri ≈ 0.1 and the local shear is amplified approximately five-fold relative to the initial primary shear, making the secondary KH instability both more weakly stratified than its parent and faster in timescale.

These findings support the view, developed in earlier work (Caulfield & Peltier, 2000; Klaassen & Peltier, 1985, 1989, 1991; Mashayek & Peltier, 2012a, 2012b), that the emergence of higher-order instabilities is primarily controlled by Re. With the parameters of this simulation, however, tertiary instabilities are not observed at cm scale. Although by $t = 50$ s the secondary braids between the secondary billows have sharpened by another order of magnitude to 2 mm (not shown, but still comfortably resolved by our stretched grid), the primary braid scale Reynolds number remains only Re ~ 5000, too low for shear to overcome strain and sustain another instability cycle. We conclude that triggering tertiary instabilities before secondary billow overturn and turbulence may require sharper secondary braids made possible by a higher large-scale Re $> 10^6$ typical of deeper environments (see Appendix A).

5.2. Braid Turbulence Energetics and Visualization From Laboratory Experiments

What happens after the transition to 3D turbulence? Our multibeam observations showed that mixing is typically sustained for periods of $\approx$5 s, corresponding to $\approx$10–20 braid shear timescales (Figures 13 and 14). To probe this regime, we now combine observations, simulations, and laboratory experiments, as sketched in Figure 16. Braid

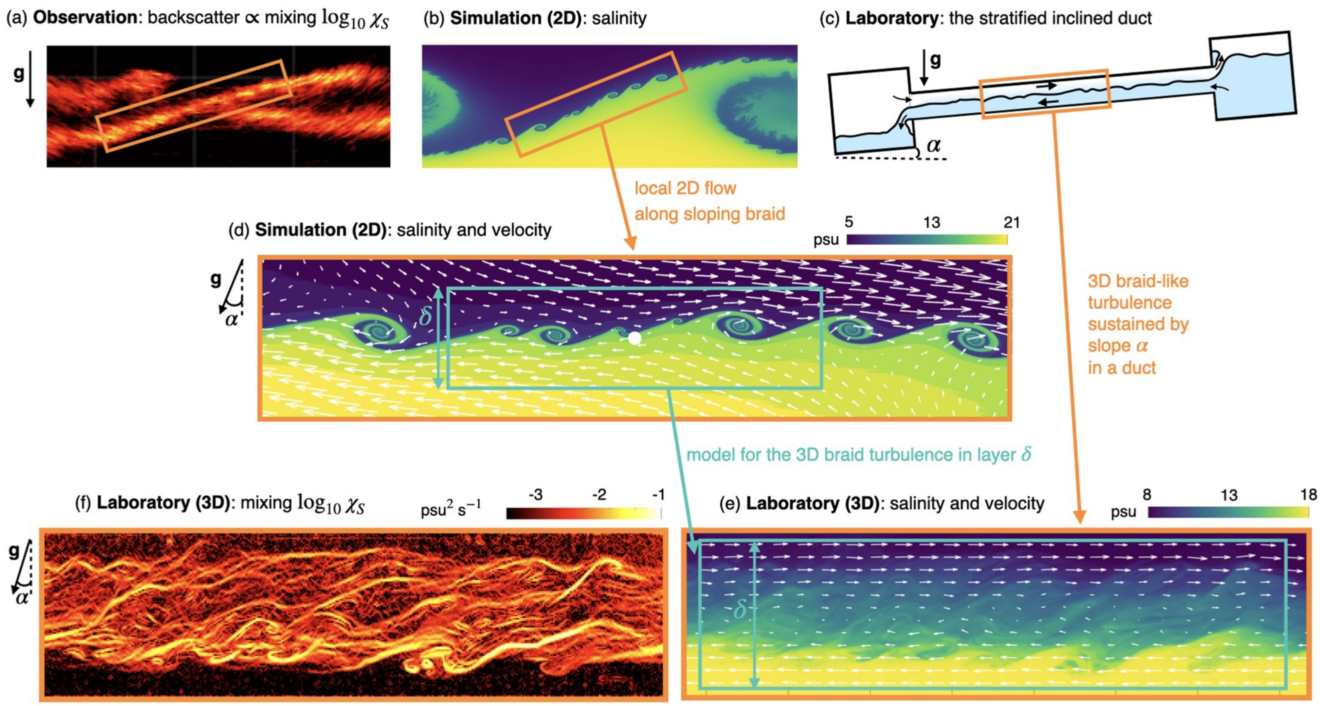

Figure 16. Bridging the gap to the smallest mixing scales by combining insights from (a) multibeam echosounder observations, (b, d) 2D direct numerical simulations, and (c, e, f) laboratory experiments. The stratified inclined duct (SID) setup (c) produces high-resolution salinity and velocity data (e, velocity vectors subsampled) in baroclinically forced stratified turbulence characteristic of the braid after the onset of secondary instability (d). SID data yield χ_s snapshots (f, here shown at the same instant as e), which serve as a model for braid mixing below the resolution of the observations in (a). In this experiment the duct height was 0.045 m, giving an effective shear layer—or "braid"—with $\delta = 0.04$ m (see cyan box in e); $\Delta U = 0.12$ m s^{-1}; and $\alpha = 0.1$, resulting in a local Re $\approx$ 1,200 and Re$_b$ $\approx$ 25, that is roughly an order of magnitude below the lower end of real braids. For further details, see main text and Lefauve (2024, Figure 7).

turbulence persists when local baroclinic production balances turbulent dissipation, the same mechanism invoked at the estuarine scale in Equation 7. This balance rests on three assumptions: (a) approximate homogeneity along the braid (valid away from curvature and eyelids; see Figure 16a); (b) approximate stationarity (valid during periods of nearly constant slope and turbulence intensity, observed in the multibeam sequences); and (c) negligible strain compared to shear (a prerequisite for secondary instability, see Figure 16b). This continuously forced turbulent state has been reproduced in the stratified inclined duct (SID) laboratory experiment (see Figure 16c). The SID drives a pure baroclinic exchange flow through a long, sloping duct connecting two reservoirs of different salinity (Lefauve & Linden, 2020; Meyer & Linden, 2014), conceptually similar to Thorpe's classic tilted-tube experiments (Thorpe, 1971) but sustained for hundreds of shear times.

The SID experiment enables detailed, non-intrusive optical measurements of turbulence energetics, with time-resolved, 3D velocity and salinity fields resolved down to the Kolmogorov scale using simultaneous stereo particle image velocimetry and laser-induced fluorescence (Partridge et al., 2019). As reviewed in Lefauve (2024), these measurements show that the turbulence within the duct interior also satisfies Equation 7 under the same assumptions, making it a faithful laboratory analog for braid turbulence. This analogy is illustrated in Figures 16d and 16e by comparing the braid-scale salinity and velocity from simulation at the onset of secondary instability (panel d) with those from the laboratory during sustained turbulence (panel e), both shown in the local frame sloping at angle α. The cyan boxes highlight the shear layer (braid) thickness δ where the analogy holds. A few braid shear times after the onset of secondary KH instability (panel d), this region is expected to transition to 3D turbulence and enter the SID-like regime away from boundaries (panel e). This equilibrium corresponds to the mature braid, where dissipation ϵ and mixing χ_s peak, as in the brightest signal in the multibeam sequences.

These laboratory observations allow us to formulate a physics-based predictive model for ϵ and χ_s used in this paper. The turbulent kinetic energy dissipation in the braid was confirmed by SID data and supporting modeling was confirmed to be (Lefauve & Linden, 2022b, Section 3; Zhu et al., 2023, Section 5.4):

$$\epsilon \approx \frac{1}{16}\alpha\,\mathrm{Ri}\,(1-\Gamma)\frac{(\Delta U)^3}{\delta}. \tag{13}$$

Equation 13 is adapted from Lefauve (2024, Equation 6) but is written here in physical units. Across the braid, the gradient Richardson number is expected to be $\mathrm{Ri} \approx 0.1\text{–}0.15$, matching the turbulent equilibrium found in SID experiments (Lefauve & Linden, 2022a), confirmed by DNS of SID (Zhu et al., 2023), and by higher-Re_b DNS in a similar shear-forced regime (Portwood et al., 2019). This range of Ri is also consistent with the peak in the pycnocline-scale histogram of $\min_z \mathrm{Ri}$ (Figure 8b), where even at larger scales, continuous shear forcing sustains Ri well below marginal instability. The mixing coefficient, or efficiency, is classically defined as $\Gamma = B/\epsilon$, where B is the irreversible buoyancy flux. Under statistically steady conditions with negligible transport terms and constant background N^2, the destruction rate of buoyancy variance χ is in lock-step with B, so that $B \approx \chi$ and $\Gamma \approx \Gamma_\chi$ (Caulfield, 2020). This efficiency is tightly linked to Ri through the turbulent Prandtl number $\mathrm{Pr_T}$, defined as the ratio of the eddy viscosity ν_T to the turbulent diffusivity for density K_ρ:

$$\mathrm{Pr_T} = \frac{\nu_T}{K_\rho} = \frac{P/S^2}{B/N^2} = \frac{\Gamma\,\mathrm{Ri}^{-1}}{1+\Gamma} \qquad \text{hence} \qquad \Gamma_\chi \approx \Gamma = \frac{\mathrm{Ri}}{\mathrm{Pr_T}-\mathrm{Ri}} \approx 0.11\text{–}0.18, \tag{14}$$

using the expected range $\mathrm{Ri} \approx 0.1\text{–}0.15$ and $\mathrm{Pr_T} \approx 1$. A turbulent Prandtl number close to unity is supported both by measurements in the Connecticut River estuary (Holleman et al., 2016) and high-Re_b, shear-forced DNS (Portwood et al., 2019), which showed that the turbulent processes that diffuse buoyancy and momentum in this regime are highly coupled and not substantially affected by the stratification. Assuming a braid-average $\Gamma \approx \Gamma_\chi \approx 0.15$, we can now estimate dissipation and mixing at the braid scale as

$$\epsilon \approx 0.05\,\alpha\,\mathrm{Ri}\,\frac{(\Delta U)^3}{\delta} \approx 0.007\,\alpha\,\delta^2 S^3 \approx 1\times10^{-4} - 4\times10^{-3}\ \mathrm{m^2\,s^{-3}}, \tag{15}$$

$$\chi_s \approx \frac{N^2}{(g\beta)^2}\Gamma_\chi\,\epsilon \approx 0.001\,(g\beta)^{-2}\,\alpha\,\delta^2 N^2 S^3 \approx 1\times10^{-2} - 2\times10^{1}\ \mathrm{psu^2\,s^{-1}}. \tag{16}$$

Note that Equation 15 provides the correct pre-factor (0.05) to the earlier scaling Equation 8. To estimate the range in ϵ and χ_s in our data, we used for the braid $\alpha = 0.2\text{–}0.4$, $\delta = 0.1\text{–}0.15$ m, $S \approx 2\text{–}4\ \mathrm{s^{-1}}$ and $N \approx 0.7\text{–}1.4\ \mathrm{s^{-1}}$. The resulting braid dissipation predicted by Equation 15 reaches values over two orders of magnitude larger than the pycnocline-averaged estimate in Section 3.2, as the enhanced braid α and S more than compensate for the smaller δ (noting that $\epsilon \propto \alpha\,\delta^2 S^3$). The braid mixing estimates from Equation 16 are up to four orders of magnitude above background levels owing to the simultaneous enhancement of ϵ and N (noting that $\chi_s \propto \alpha\,\delta^2 S^5$ at constant Ri). Recalling Equation 5, this enhancement is also consistent with the ≈20 dB increase in acoustic scattering observed in our data. The predicted ranges in Equations 15 and 16 are consistent with several independent observations in this estuary including peak ϵ values in Lavery et al. (2013, Figure 8a), Holleman et al. (2016, Figure 7a) and braid-scale ϵ and χ_s values in Geyer et al. (2010, Table 1).

To quantify the inertial range below the braid scale, we estimate the range of buoyancy Reynolds numbers as

$$\mathrm{Re_b} \approx 200\text{–}2{,}000. \tag{17}$$

The lower value corresponds to the thinner, shallower, and more weakly stratified braids, while the upper value to the thicker, steeper, and more strongly stratified ones. This range is comparable to the large-scale estimate $\mathrm{Re_b} \approx 300\text{–}3{,}000$ (Equation 12), reflecting the fact that both ϵ and N increase with the enhanced braid shear S, since Ri remains approximately constant across scales under continuous shear forcing. Furthermore, Equation 15 implies a direct relation between the local $\mathrm{Re_b}$ and Re (recalling that the latter is based on half the velocity differential and layer thickness)

$$\mathrm{Re_b} = \frac{\epsilon}{\nu N^2} \approx 0.05\,\alpha\,\frac{\Delta U\,\delta}{\nu} \approx 0.2\,\alpha\,\mathrm{Re}, \tag{18}$$

which holds both at the large pycnocline scale, where $\alpha = 0.002\text{–}0.02$ and $\mathrm{Re} = 8\times10^5$ yielded Equation 12 and at the braid scale, where $\alpha = 0.2\text{–}0.4$ and $\mathrm{Re} = 5{,}000\text{–}25{,}000$ yield Equation 17. In other words, the small-scale braids achieve $\mathrm{Re_b}$ comparable to the large-scale pycnocline because their steeper slope α compensates for their lower Re.

We conclude this section with the final key question of the paper: what does mixing look like at scales far below the resolution of field measurements, down to the Kolmogorov scale? Specifically, do we find evidence of secondary KH billows overturning within the lower-Re braid—that is small "bright cores"—as would be inferred from the unforced case? Laboratory data provide the answer, resolving χ_s down to <0.1 mm in Figure 16f. (See also Lefauve (2024, Figure 7) for corresponding snapshots of other flow variables including ϵ.) The dominant structures are long and thin filaments reminiscent of stacked braids but at much smaller scales (thickness $<\delta/25$). Crucially, these high-χ_s filaments remain relatively flat and statically stable, without evidence of elevated χ_s in overturning billows. In this snapshot, we find that the peak value within filaments is $\chi_s \approx 10^{-1}$ psu^2 s^{-1} (bright yellow shades), one and a half orders of magnitude above the mean $\chi_s \approx 10^{-2.5}$ psu^2 s^{-1} (red shades). Such extreme concentration of scalar variance dissipation at high Sc is consistent with emerging evidence from DNS (Petropoulos et al., 2024), though these DNS were limited to Sc $= 7$ (thermally stratified water) and did not include mean shear.

Thus the structures shown in Figure 16f are a valuable laboratory analog for the plausible structure well below the resolution of the acoustics in Figure 16a. However, the exact scale separation between the braid thickness δ and the finer filaments is likely controlled by the braid dynamic range $\mathrm{Re_b}$. This experiment has $\mathrm{Re_b} \approx 25$, an order of magnitude below the lowest braid-scale value expected in our field data (recall Equation 17). In this sense, the scale separation seen here is a lower bound of what occurs in reality, where thicker and steeper braids would generate even thinner and more extreme χ_s filaments. Our key conclusion, however, remains robust—when sustained by baroclinic forcing over many shear timescales, braid mixing is not dominated by secondary overturning billow cores but by thinner and more stable filaments.

6. Conclusions

This paper proposes a new model for the energy cascade in large-scale shear instabilities with continuous baroclinic forcing. The novel use of multibeam acoustic backscatter revealed the spatial structure and temporal evolution of mixing within trains of KH instabilities in the shallow Connecticut River estuary, an ideal natural laboratory. We sampled dozens of events across four transects, combining shipboard multibeam survey and colocated ADCP/CTD profiles with a more conventional single-beam survey from an AUV (Section 2).

The large-scale hydrodynamic conditions in Section 3 show that the pycnocline in this estuary is primed for KH instability, with minimum Ri in the water column spanning 0–0.3 and peaking just below 0.15. Baroclinic forcing from tidal and bathymetric slopes steadily reduces Ri and sustains submarginal instability well below the threshold of Ri $= 0.25$, which remains a powerful predictor for the occurrence of mixing in the acoustics. This equilibrium is explained by a balance between baroclinic shear production and turbulent dissipation (Equation 7) and yields pycnocline-averaged dissipation $\epsilon \sim 10^{-5}-10^{-4}$ m^2 s^{-3} (Equation 8), in line with earlier measurements (Lavery et al., 2013). Yet these prior observations also revealed rare, localized peaks suggesting that large-scale averages conceal more intense, small-scale structures, motivating our subsequent focus on braids. The representative parameters at the estuarine scale (Ri $= 0.15$, Re $= 8 \times 10^5$, Sc ≈ 700) imply a turbulent cascade spanning from the meter scale to tens of microns (Equation 11)—a high dynamic range controlled by $\mathrm{Re_b} \approx 300-3{,}000$ (Equation 12). These values confirm that the flow sits firmly in the regime of intense stratified turbulence, with broad relevance to mixing hotspots far beyond this single estuary.

The smaller-scale multibeam observations in Section 4 characterize the spatial structure and lifecycle of mixing within KH billow trains, confirming and refining the picture previously inferred from single-beam and braid-resolving finescale measurements (Geyer et al., 2010; Vladoiu et al., 2025). Intense mixing is not usually generated by primary core overturn at the meter scale, as in lower-Re studies, but is instead concentrated along thin ($\approx 5-15$ cm) sloping braids with moderate slopes $\alpha \approx 0.2-0.4$ which extend into flatter eyelids. These braids steepen, spawn secondary billows, and grow thicker by intense turbulence, which is sustained and advected along the eyelids before decaying, typically over only ≈ 5 s (a few shear time scales)—an order of magnitude faster than the lifecycle of idealized, lower-Re KH billows. At times, eyelid turbulence detaches and interacts with neighboring wavelengths or rolls up into the primary core, highlighting the diversity of short-lived processes. Yet across many events, the consistent picture of braid-generated, eyelid-advected turbulence establishes it as the dominant high-Re mixing process. We emphasize that multibeam imagery was critical to reaching this conclusion, since single-beam systems used in past studies conflate space and time through the relative motion of the platform and the instabilities, obscuring both slopes (billow aspect ratio) and evolution.

The modeling in Section 5 explains why mixing originates in braids and how it cascades below observational resolution. Our 2D DNS in Section 5.1 at field-matched (Ri, Re, Sc) shows that as braids steepen, baroclinic forcing of shear (Equation 6) and strain-induced compression sharpen the pycnocline until shear dominates and secondary KH appears at the braid scale ($\delta \approx 10$ cm). The secondary KH mechanism is established in the literature, but our highly-resolved DNS provides mechanistic support of its rapid onset and relevance at field parameters. Secondary KH instability is thought to pre-empt primary KH core overturn and shortcut the transition to 3D turbulence because it evolves on faster timescales, due to the amplification of braid shear at high estuarine $\mathrm{Re} \sim 10^6$. Tertiary KH instability does not generically arise at this Re due to insufficient sharpening of the braids between secondary billows, but it is expected at higher Re.

The analysis of the ensuing braid stratified turbulence regime in Section 5.2 completes this picture. After the fast 3D collapse of secondary billows, a turbulent braid with local $\mathrm{Re} \sim 10^3 - 10^4$ persists for many local shear times in baroclinic-production–dissipation balance (Equation 7). This balance mirrors that of the main pycnocline at smaller scale and steeper slope, and yields predictions for the braid dissipation ϵ (Equation 15) and mixing χ_s (Equation 16) as functions of local slope, shear and thickness that are quantitatively consistent with the acoustics and with the elevated in-situ values of prior studies. Although evaluated here using parameters derived from our estuarine observations, these relations are generic to baroclinically-forced stratified turbulence and may be applied to other environments (Appendix A) wherever these quantities can be estimated. In this sense, our braid-based ϵ estimates offer an alternative to Thorpe-scale estimates that infer ϵ from density overturns associated with primary KH billows (see Thorpe, 2005, Section 6.3.2; Vladoiu et al., 2025). Despite the braids and eyelids exhibiting ϵ orders of magnitude above the large-scale pycnocline, their dynamic range $\mathrm{Re_b} \approx 200-2{,}000$ (Equation 17), remains comparable to the large-scale value (Equation 18) because N^2 increases with S^2 at roughly constant $\mathrm{Ri} \approx 0.1-0.15$ across scales. The enhanced braid ϵ is thought to arrest the primary KH growth beyond $\alpha \approx 0.4-0.5$ and prevent overturn, but this conjecture is left for future work.

The baroclinic-production–dissipation balance is also reproduced in the SID experiment—a sustained downslope baroclinic exchange flow—at braid-matched Ri, Re, and Sc. High-resolution optical measurements in SID extend our view of the cascade below the braid scale, resolving sub-mm structures across the inertial subrange. The experimental data reveal that even at the small dissipative scales, peak mixing does not occur in overturns (bright cores), but in thin, relatively flat, sheared filaments, where χ_s vastly exceeds the braid-average. Because the experiment shown operated at the lower end of the expected braid $\mathrm{Re_b}$, the separation between braid and filament scales—and the associated mixing levels—should be even sharper in the field than visualized here.

7. Implications

The first implication of these results concerns the qualitative structure of density interfaces in high-Re, forced environments. Even under vigorous shear instabilities, estuarine pycnoclines rarely show steps; instead they remain close to a smooth, hyperbolic-tangent form. A step-like structure with a central mixed layer would be expected if mixing were dominated by intermittent large overturns in the billow cores, as in lower-Re, unforced flows. Instead, smaller-scale braid and eyelid mixing along the flanks of billows continually entrains fluid at the edges of the pycnocline, broadening the interface smoothly without ever carving out a central mixed layer. Future work should estimate what fraction of global ocean mixing occurs in this regime; the gallery of observations in Appendix A suggests that this regime is widespread.

The second implication concerns mixing efficiency Γ and how closures represent Ri-dependent stability functions. We revealed a sustained baroclinic production–dissipation balance with local $\mathrm{Ri} \approx \Gamma \approx 0.1-0.15$ at both the main pycnocline and the finer braid scales, below the canonical $\mathrm{Ri} = 0.25$ and $\Gamma = 0.2$ (Gregg et al., 2018; Holleman et al., 2016). These lower values, however, may not represent the event-integrated mixing of the primary KH train. If the averaging aperture is widened to include the full pycnocline and primary instability lifecycle—as may be more typical of available model resolution—Ri and Γ may rise toward the canonical values, so the bulk Γ may be more reflective of the marginal Ri that triggers the instability than the local submarginal Ri at peak shear and mixing. Closures for continuously forced mixing hotspots may need to account for such a resolution-dependence of stability threshold and mixing efficiency.

The third implication, which is related, concerns how dissipation and mixing are predicted and interpreted across scales in field observations. Our baroclinic production–dissipation balance provides practical predictions for pycnocline- and braid-scale ϵ and χ from local slope, shear, and length scales. Yet even the braid-scale ϵ and χ average over myriad extreme filaments beyond the reach of microstructure and micro-CTD profilers, raising the question of what is actually being averaged over in field data, depending on their spatio-temporal resolution. Our results also suggest that the fine-scale cascade may remain Re-dependent even at very high Re.

Appendix A: Gallery of Field Observations of KH Instabilities

Figure A1 gives an overview of KH visualizations around the world's oceans, reproducing snapshots from the literature and additional data sets provided by the co-authors. Though most cases were captured with single-beam echosounders, panel (d) is an early multibeam record and the deeper-ocean examples (panels l, m, and u) used

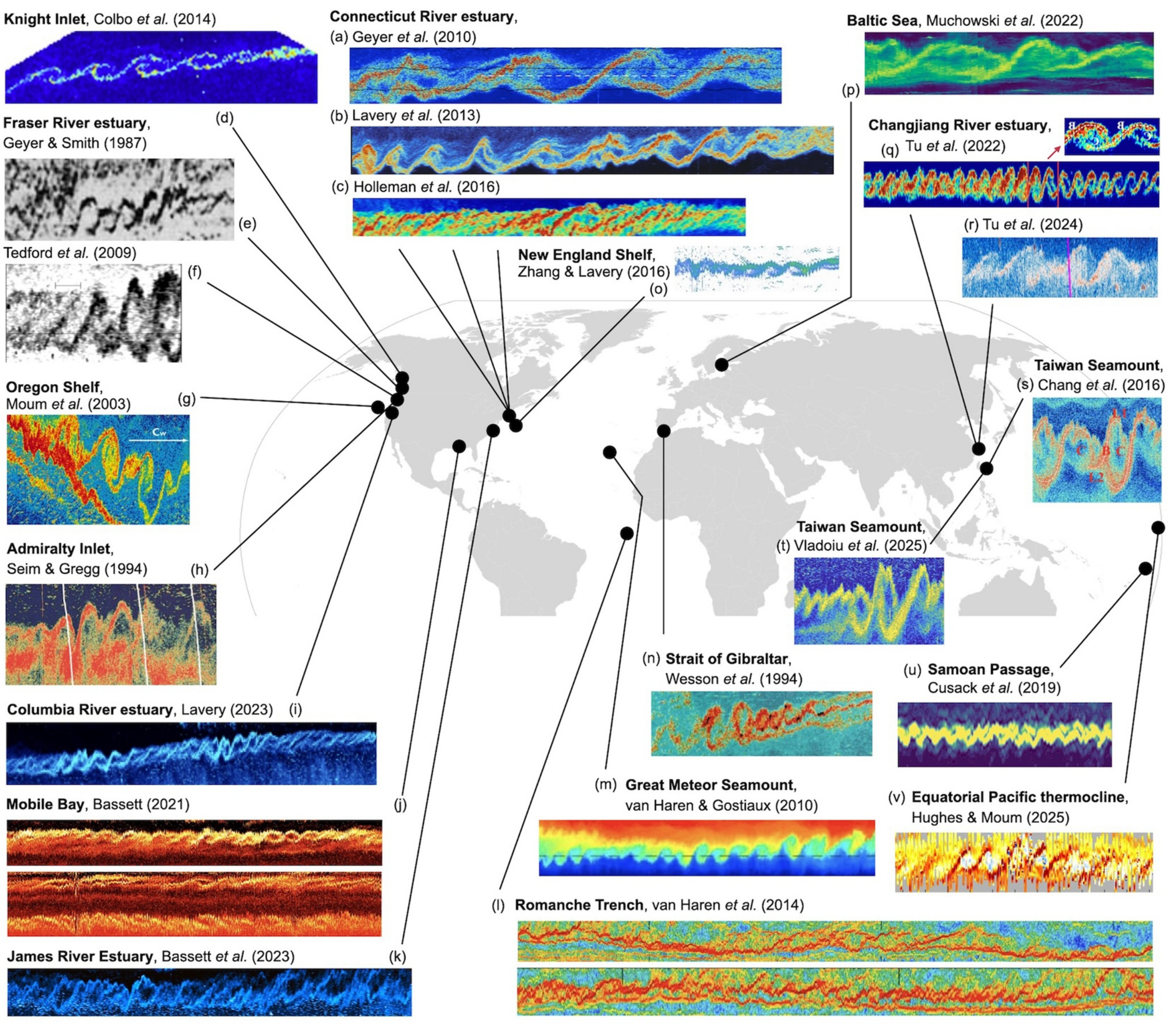

Figure A1. Visualizations of KH instabilities, showing the wide relevance of braid-driven mixing in hotspots with continuous shear forcing, with the possible exception of a more transient internal wave overturn in (g). The signal typically shows either scalar microstructure inferred from acoustic backscatter or the vertical temperature gradient, except panel (m), which shows temperature itself. Panel (a) adapted from Colbo et al. (2014), with permission from Elsevier. Panels (g, p, t) adapted from Moum et al. (2003), Muchowski et al. (2022), and Vladoiu et al. (2025), © American Meteorological Society. Used with permission. See text for details and references.

moored thermistor arrays, panel (v) used wave-pumped χ pods. The details of some of these observations are tabulated in Tu et al. (2020, Table 1). Although the direction of the shear varied among studies—and thus the left-right orientation of the braids—here we flipped them to be consistent with our convention ($\partial U/\partial z > 0$ and braid slope $\alpha > 0$). The only exception is the lower image in panel (j), where two trains of instabilities formed simultaneously on stacked pycnoclines with shear in opposite directions. Note that in all panels (except d), the lack of multibeam imagery means actual braid slopes and aspect ratios are unknown and typically appear exaggerated, due to inevitable acquisition distortion and arbitrary scaling in these space–time plots.

Three key points emerge from Figure A1. First, the KH instability is a ubiquitous mixing process, occurring in a variety of environments, depths, and modes of stratification, including:

- *Salinity stratification (pycnoclines)* in estuaries and straits, such as in panels (a-c) the Connecticut River salt-wedge estuary (Geyer et al., 2010; Holleman et al., 2016; Lavery et al., 2013); (d) the Knight inlet, a tidally driven fjord (Colbo et al., 2014); (e,f) the Fraser River estuary (Geyer & Smith, 1987; Tedford et al., 2009); (h) the Admiralty inlet (Seim & Gregg, 1994); (i) the Columbia River estuary; (j) the Mobile Bay estuary; (k) the James River estuary (Bassett et al., 2023); (n) the Strait of Gibraltar (Wesson & Gregg, 1994) and (r) the Kuroshio intrusion into the Changjiang River plume (Tu et al., 2024);
- *Temperature stratification (thermoclines)*, such as in (g) the Oregon continental shelf (Moum et al., 2003); (o) the Gulf Stream along the New England shelf break (disregarding the small-scale, uncorrected fluctuations of the braid from the heave of the boat); (l) the deep downslope channel flow of Antarctic Bottom Water through the Romanche Trench (displaying buoyancy frequency N) (van Haren et al., 2014); (m) the tidally driven downslope flow above Great Meteor Seamount (displaying temperature) (van Haren & Gostiaux, 2010); (p) the northern Baltic Sea above a sill (Muchowski et al., 2022); (s,t) the Kuroshio above a seamount off southeastern Taiwan (Chang et al., 2016; Vladoiu et al., 2025); (u) the deep overflow in the Samoan Passage (Cusack et al., 2019); (v) the equatorial Pacific thermocline (Hughes & Moum, 2025);
- *Sediment-induced stratification (lutoclines)* in highly turbid estuaries such as in (q) the Changjiang river (Tu et al., 2022).

Second, KH billows occur across a wide range of scales, with vertical amplitudes spanning three orders of magnitude: from $\delta \approx 0.5$–2 m in shallow estuaries (panels a–c, e, f, q, r, and j) and the open ocean (v), to 5–20 m in deeper estuaries and coastal seas (d, g–i, k, and p), and to 50–200 m in the Strait of Gibraltar (n) and in the open ocean (l-m, and s-u). Typical velocity scales vary much less, and tend to be of order $\Delta U \sim 1$ m s^{-1} across studies. This implies a range of Reynolds numbers Re $\sim 10^5 - 10^8$, with turbulence likely triggered by secondary instabilities at the lower Re (coastal ocean) and by tertiary instabilities at the higher Re (deep ocean).

Third, the typical structure of high-Re mixing observed and explained in this paper—"bright" baroclinic braids connecting quiet "dark" cores—appears generic. The notable exception is the internal solitary wave propagating shoreward over the Oregon shelf (panel g), where the primary billow overturns and mixes significantly. We attribute this to the transient, time-dependent shear and steepening of solitary waves, in contrast with the more steady shear forcing assumed in our braid-mixing model and dominant in other observations.

Appendix B: Motion Correction of the Multibeam Echosounder Data

Due to the lack of a tightly integrated inertial navigation system on the multibeam platform, the pitch and heave estimates were performed in a data-driven manner. Here, the specular bottom reflection was used to estimate the motion. The lack of a bathymetric prior meant that two assumptions were made: (a) the pitch and heave of the system were slow compared to the ping rate and (b) changes in the local bathymetry and bathymetry corresponding slopes were slow compared to the pitch and heave. Given the sampling rate of 17 Hz, even short period waves large enough to impact the vessel operations are roughly two orders of magnitude slower than the ping rate. The location of the bottom reflection was tracked using 2D normalized cross-correlations of each ping and nearest 20 neighbors in the polar domain (multibeam azimuth and range). This results in a series of estimates for the azimuthal and range shift of the bottom reflections between each ping and those neighbors. These estimates are then converted to a single motion solution using an iteratively reweighted least squares maximum likelihood estimator. Finally, the motion solution was band-pass filtered to both remove long-term drift (the heave and pitch should both oscillate about neutral) and high-frequency components corresponding to non-physically fast changes in multibeam position and orientation. The various estimator and filter parameters required tuning and were chosen heuristically; any grossly inaccurate motion estimates were rapidly apparent in the multibeam imagery.

Appendix C: Numerical Simulation Method

The 2D DNS presented in Section 5.1 were performed with the Julia package `Oceananigans.jl` (Ramadhan et al., 2020). The base state consists of hyperbolic-tangent velocity and salinity profiles inspired by the field profiles of Figure 7:

$$u(z,0) = 0.5\tanh(2z)\ \mathrm{m\ s^{-1}}, \qquad s(z,0) = 13 - 10\tanh(2z)\ \mathrm{psu}, \tag{C1}$$

with buoyancy $b = g\beta(13 - s)$ over a vertical domain $z \in [-2.5, 2.5]$ m (total depth 5 m). These dimensional forms are shown for clarity and correspond to the results plotted in Figure 15.

The simulation solved the incompressible, non-hydrostatic Navier–Stokes equations under the Boussinesq approximation, given in dimensionless form by

$$\tilde{\nabla}\cdot\tilde{\mathbf{u}} = 0, \qquad \frac{\partial\tilde{\mathbf{u}}}{\partial\tilde{t}} + \tilde{\mathbf{u}}\cdot\tilde{\nabla}\mathbf{u} = -\tilde{\nabla}\tilde{p} + \frac{1}{\mathrm{Re}}\tilde{\nabla}^2\tilde{\mathbf{u}} + Ri\,\tilde{b}\,\mathbf{e}_z, \qquad \frac{\partial\tilde{b}}{\partial\tilde{t}} + \tilde{\mathbf{u}}\cdot\tilde{\nabla}\tilde{b} = \frac{1}{\mathrm{Re\,Sc}}\tilde{\nabla}^2\tilde{b}, \tag{C2}$$

with parameters $(\mathrm{Re}, \mathrm{Ri}, \mathrm{Sc})$ given by Equation 10. The solver used finite-volume discretization, WENO advection, and third-order Runge–Kutta timestepping on an Nvidia A100 GPU (40 GB).

Free-slip and no-flux boundary conditions were imposed at the top and bottom, and periodic boundary conditions were applied in x. Although Figure 15 shows two wavelengths for clarity, only a single wavelength was simulated, which is sufficient since vortex pairing is irrelevant at the high Re considered.

An initial perturbation was imposed as the fastest-growing linear mode (wavelength 6.5 m) with energy (defined as the domain-averaged $(1/2)(u^2 + w^2 + b^2)$) equal to 10^{-4} of the base flow, plus white noise with energy equal to 10^{-3} of the base flow—still moderate compared to expected field levels.

A stretched vertical grid ($12,000 \times 12,000$ points in x and z) was used to capture sharp gradients at the braid scale and ensure convergence. In physical units, the horizontal grid spacing was $\Delta x = 0.54$ mm, the vertical spacing averaged $\Delta z = 0.42$ mm, and reached a minimum $\Delta z = 0.21$ mm at $z = 0$.

Conflict of Interest

The authors declare no conflicts of interest relevant to this study.

Availability Statement

The data and code used in this study are publicly archived in the repository (Lefauve et al., 2026). This includes all field data from transects T0–T3, multibeam movies, the simulation code, experimental data as well as high-resolution and supplementary figures.

Acknowledgments
We thank C. P. Caulfield, S. F. Lewin and E. R. Bouckley for discussions on secondary KH instability at the WHOI Geophysical Fluid Dynamics Program supported by the NSF and ONR. We thank A. Atoufi, J. R. Taylor, S. F. Lewin and E. R. Bouckley for sharing code that was adapted for the simulations. Computing was performed on the Delta HPC at the University of Illinois Urbana-Champaign, supported by the NSF and the State of Illinois. Lefauve was supported by a NERC Independent Research Fellowship NE/W008971/1. Bassett, Plotnick, Lavery and Geyer were supported by ONR Grants N00014-16-1-2948 and N00014-19-1-2593. We thank the authors of previous studies for permission to reuse selected material in Figure A1. ChatGPT (OpenAI) was used for minor language editing.

References

Bak, P., Tang, C., & Wiesenfeld, K. (1988). Self-organized criticality. *Physical Review A*, *38*(1), 364–374. https://doi.org/10.1103/physreva.38.364

Bartello, P., & Tobias, S. M. (2013). Sensitivity of stratified turbulence to the buoyancy Reynolds number. *Journal of Fluid Mechanics*, *725*, 1–22. https://doi.org/10.1017/jfm.2013.170

Bassett, C., Lavery, A. C., Petitt, R., & Loranger, S. (2022). Autonomous platforms for measuring broadband backscatter. *Proceedings of Meetings on Acoustics*, *45*(1), 005002. https://doi.org/10.1121/2.0001654

Bassett, C., Lavery, A. C., Ralston, D., Geyer, W. R., Jurisa, J. T., Thomson, J., et al. (2023). Acoustic backscattering at a tidal intrusion front. *Progress in Oceanography*, *219*, 103167. https://doi.org/10.1016/j.pocean.2023.103167

Carpenter, J. R., Balmforth, N. J., & Lawrence, G. A. (2010). Identifying unstable modes in stratified shear layers. *Physics of Fluids*, *22*(5), 054104. https://doi.org/10.1063/1.3379845

Carpenter, J. R., Tedford, E. W., Rahmani, M., & Lawrence, G. A. (2010). Holmboe wave fields in simulation and experiment. *Journal of Fluid Mechanics*, *648*, 205–223. https://doi.org/10.1017/S002211200999317X

Caulfield, C. P. (1994). Multiple linear instability of layered stratified shear flow. *Journal of Fluid Mechanics*, *258*, 255–285. https://doi.org/10.1017/s0022112094003320

Caulfield, C. P. (2020). Open questions in turbulent stratified mixing: Do we even know what we do not know? *Physical Review Fluids*, *5*(11), 110518. https://doi.org/10.1103/physrevfluids.5.110518

Caulfield, C. P. (2021). Layering, instabilities, and mixing in turbulent stratified flows. *Annual Review of Fluid Mechanics*, *53*(1), 113–145. https://doi.org/10.1146/annurev-fluid-042320-100458

Caulfield, C. P., & Peltier, W. R. (2000). The anatomy of the mixing transition in homogeneous and stratified free shear layers. *Journal of Fluid Mechanics*, *413*, 1–47. https://doi.org/10.1017/s0022112000008284

Chang, M. (2021). Marginal instability within internal solitary waves. *Geophysical Research Letters*, *48*(9), e2021GL092616. https://doi.org/10.1029/2021GL092616

Chang, M., Jheng, S., & Lien, R. (2016). Trains of large Kelvin-Helmholtz billows observed in the Kuroshio above a seamount. *Geophysical Research Letters*, *43*(16), 8654–8661. https://doi.org/10.1002/2016GL069462

Cimoli, L., Mashayek, A., Johnson, H. L., Marshall, D. P., Naveira Garabato, A. C., Whalen, C. B., et al. (2023). Significance of diapycnal mixing within the Atlantic meridional overturning circulation. *AGU Advances*, *4*(2), e2022AV000800. https://doi.org/10.1029/2022AV000800

Colbo, K., Ross, T., Brown, C., & Weber, T. (2014). A review of oceanographic applications of water column data from multibeam echosounders. *Estuarine, Coastal and Shelf Science*, *145*, 41–56. https://doi.org/10.1016/j.ecss.2014.04.002

Corcos, G. M., & Sherman, F. S. (1976). Vorticity concentration and the dynamics of unstable free shear layers. *Journal of Fluid Mechanics*, *73*(2), 241–264. https://doi.org/10.1017/S0022112076001365

Cusack, J. M., Voet, G., Alford, M. H., Girton, J. B., Carter, G. S., Pratt, L. J., et al. (2019). Persistent turbulence in the Samoan passage. *Journal of Physical Oceanography*, *49*(12), 3179–3197. https://doi.org/10.1175/JPO-D-19-0116.1

D'Asaro, E. A. (2022). How do internal waves create turbulence and mixing in the ocean? [preprint]. *ESS Open Archive*. https://doi.org/10.1002/essoar.10511843.1

Dritschel, D. G., Haynes, P. H., Juckes, M. N., & Shepherd, T. G. (1991). The stability of a two-dimensional vorticity filament under uniform strain. *Journal of Fluid Mechanics*, *230*, 647–665. https://doi.org/10.1017/S0022112091000826

Gargett, A. E., Osborn, T. R., & Nasmyth, P. W. (1984). Local isotropy and the decay of turbulence in a stratified fluid. *Journal of Fluid Mechanics*, *144*, 231–280. https://doi.org/10.1017/S0022112084001592

Geyer, W. R., Lavery, A. C., Scully, M. E., & Trowbridge, J. H. (2010). Mixing by shear instability at high Reynolds number. *Geophysical Research Letters*, *37*(22), 2010GL045272. https://doi.org/10.1029/2010GL045272

Geyer, W. R., Ralston, D. K., & Holleman, R. C. (2017). Hydraulics and mixing in a laterally divergent channel of a highly stratified estuary. *Journal of Geophysical Research: Oceans*, *122*(6), 4743–4760. https://doi.org/10.1002/2016JC012455

Geyer, W. R., Scully, M. E., & Ralston, D. K. (2008). Quantifying vertical mixing in estuaries. *Environmental Fluid Mechanics*, *8*(5–6), 495–509. https://doi.org/10.1007/s10652-008-9107-2

Geyer, W. R., & Smith, J. (1987). Shear instability of a highly stratified estuary. *Journal of Physical Oceanography*, *17*(10), 1668–1679. https://doi.org/10.1175/1520-0485(1987)017<1668:siiahs>2.0.co;2

Gregg, M. C., D'Asaro, E. A., Riley, J. J., & Kunze, E. (2018). Mixing efficiency in the ocean. *Annual Review of Marine Science*, *10*(1), 443–473. https://doi.org/10.1146/annurev-marine-121916-063643

Hasegawa, D., Matsuno, T., Tsutsumi, E., Senjyu, T., Endoh, T., Tanaka, T., et al. (2021). How a small reef in the Kuroshio cultivates the ocean. *Geophysical Research Letters*, *48*(7), e2020GL092063. https://doi.org/10.1029/2020GL092063

Hazel, P. (1972). Numerical studies of the stability of inviscid stratified shear flows. *Journal of Fluid Mechanics*, *51*(1), 39–61. https://doi.org/10.1017/s0022112072001065

Hoecker-Martínez, M. S., & Smyth, W. D. (2012). Trapping of gyrotactic organisms in an unstable shear layer. *Continental Shelf Research*, *36*, 8–18. https://doi.org/10.1016/j.csr.2012.01.003

Holleman, R. C., Geyer, W. R., & Ralston, D. K. (2016). Stratified turbulence and mixing efficiency in a salt wedge Estuary. *Journal of Physical Oceanography*, *46*(6), 1769–1783. https://doi.org/10.1175/JPO-D-15-0193.1

Howard, L. N. (1961). Note on a paper of John W. Miles. *Journal of Fluid Mechanics*, *10*(4), 509–512. https://doi.org/10.1017/S0022112061000317

Hughes, K. G., & Moum, J. N. (2025). Imaging thermocline microstructure in 2d with swaths traced by wave-pumped χ pods. *Journal of Geophysical Research: Oceans*, *130*(4), e2024JC022134. https://doi.org/10.1029/2024JC022134

Jackson, P. R., & Rehmann, C. R. (2014). Experiments on differential scalar mixing in turbulence in a sheared, stratified flow. *Journal of Physical Oceanography*, *44*(10), 2661–2680. https://doi.org/10.1175/JPO-D-14-0027.1

Klaassen, G. P., & Peltier, W. R. (1985). The onset of turbulence in finite-amplitude Kelvin–Helmholtz billows. *Journal of Fluid Mechanics*, *155*, 1–35. https://doi.org/10.1017/S0022112085001721

Klaassen, G. P., & Peltier, W. R. (1989). The role of transverse secondary instabilities in the evolution of free shear layers. *Journal of Fluid Mechanics*, *202*, 367–402. https://doi.org/10.1017/S0022112089001210

Klaassen, G. P., & Peltier, W. R. (1991). The influence of stratification on secondary instability in free shear layers. *Journal of Fluid Mechanics*, *227*, 71–106. https://doi.org/10.1017/S0022112091000013

Kundu, P. K., Cohen, I. M., & Dowling, D. R. (2016). *Fluid mechanics* (6th ed.). Elsevier.

Lavery, A. C., Geyer, W. R., & Scully, M. E. (2013). Broadband acoustic quantification of stratified turbulence. *Journal of the Acoustical Society of America*, *134*(1), 40–54. https://doi.org/10.1121/1.4807780

Lefauve, A. (2024). Geophysical stratified turbulence and mixing in the laboratory. *Comptes Rendus Physique*, *25*(S3), 1–29. https://doi.org/10.5802/crphys.196

Lefauve, A., Bassett, C., Plotnick, D. S., Lavery, A. C., & Geyer, W. R. (2026). Research Data supporting "The structure and lifecycle of stratified mixing by shear instabilities in continuously forced flows" [Dataset]. https://doi.org/10.82186/7q48s-2h333

Lefauve, A., & Linden, P. F. (2020). Buoyancy-driven exchange flows in inclined ducts. *Journal of Fluid Mechanics*, *893*, A2. https://doi.org/10.1017/jfm.2020.212

Lefauve, A., & Linden, P. F. (2022a). Experimental properties of continuously forced, shear-driven, stratified turbulence. Part 1. Mean flows, self-organisation, turbulent fractions. *Journal of Fluid Mechanics*, *937*, A34. https://doi.org/10.1017/jfm.2021.810

Lefauve, A., & Linden, P. F. (2022b). Experimental properties of continuously forced, shear-driven, stratified turbulence. Part 2. Energetics, anisotropy, parameterisation. *Journal of Fluid Mechanics*, *937*, A35. https://doi.org/10.1017/jfm.2022.21

Liu, C., Wang, F., Köhl, A., Wang, X., Wang, C., & Richards, K. J. (2025). Subsurface ocean turbulent mixing enhances central Pacific ENSO. *Nature Communications*, *16*(1), 2215. https://doi.org/10.1038/s41467-025-57058-4

Mashayek, A., & Peltier, W. R. (2011). Turbulence transition in stratified atmospheric and oceanic shear flows: Reynolds and Prandtl number controls upon the mechanism. *Geophysical Research Letters*, *38*(16), L16612. https://doi.org/10.1029/2011GL048542

Mashayek, A., & Peltier, W. R. (2012a). The “zoo” of secondary instabilities precursory to stratified shear flow transition. Part 1: Shear aligned convection, pairing, and braid instabilities. *Journal of Fluid Mechanics*, *708*, 5–44. https://doi.org/10.1017/jfm.2012.304

Mashayek, A., & Peltier, W. R. (2012b). The “zoo” of secondary instabilities precursory to stratified shear flow transition. Part 2: The influence of stratification. *Journal of Fluid Mechanics*, *708*, 45–70. https://doi.org/10.1017/jfm.2012.294

Melet, A. V., Hallberg, R., & Marshall, D. P. (2022). The role of ocean mixing in the climate system. In *Ocean mixing* (pp. 5–34). Elsevier. https://doi.org/10.1016/B978-0-12-821512-8.00009-8

Melvin, G., Fox, P. A., & Condiotty, J. (2012). Adaption of the M3 multi-beam sonar to fisheries applications. In *Proc. Meet. Acoust* (Vol. 17). Acoust. Soc. Am. https://doi.org/10.1121/1.4772777.070031.

Meyer, C. R., & Linden, P. F. (2014). Stratified shear flow: Experiments in an inclined duct. *Journal of Fluid Mechanics*, *753*, 242–253. https://doi.org/10.1017/jfm.2014.358

Miles, J. W. (1961). On the stability of heterogeneous shear flows. *Journal of Fluid Mechanics*, *10*(4), 496–508. https://doi.org/10.1017/s0022112061000305

Moum, J. N., Farmer, D. M., Smyth, W. D., Armi, L., & Vagle, S. (2003). Structure and generation of turbulence at interfaces strained by internal solitary waves propagating shoreward over the continental shelf. *Journal of Physical Oceanography*, *33*(10), 2093–2112. https://doi.org/10.1175/1520-0485(2003)033<2093:sagota>2.0.co;2

Muchowski, J., Umlauf, L., Arneborg, L., Holtermann, P., Weidner, E., Humborg, C., & Stranne, C. (2022). Potential and limitations of a commercial broadband echo sounder for remote observations of turbulent mixing. *Journal of Atmospheric and Oceanic Technology*, *39*(12), 1985–2003. https://doi.org/10.1175/JTECH-D-21-0169.1

Partridge, J. L., Lefauve, A., & Dalziel, S. B. (2019). A versatile scanning method for volumetric measurements of velocity and density fields. *Measurement Science and Technology*, *30*(5), 055203. https://doi.org/10.1088/1361-6501/ab0bfd

Petropoulos, N., Couchman, M. M., Mashayek, A., De Bruyn Kops, S. M., & Caulfield, C.-c. P. (2024). Prandtl number effects on extreme mixing events in forced stratified turbulence. *Journal of Fluid Mechanics*, *983*, R1. https://doi.org/10.1017/jfm.2024.110

Portwood, G. D., de Bruyn Kops, S. M., & Caulfield, C. P. (2019). Asymptotic dynamics of high dynamic range stratified turbulence. *Physical Review Letters*, *122*(19), 194504. https://doi.org/10.1103/physrevlett.122.194504

Ramadhan, A., Wagner, G. L., Hill, C., Campin, J.-M., Churavy, V., Besard, T., et al. (2020). Oceananigans.jl: Fast and friendly geophysical fluid dynamics on GPUs. *Journal of Open Source Software*, *5*(53), 2018. https://doi.org/10.21105/joss.02018

Riley, J. J., & Lindborg, E. (2008). Stratified turbulence: A possible interpretation of some geophysical turbulence measurements. *Journal of the Atmospheric Sciences*, *65*(7), 2416–2424. https://doi.org/10.1175/2007JAS2455.1

Salehipour, H., Peltier, W. R., & Caulfield, C. P. (2018). Self-organized criticality of turbulence in strongly stratified mixing layers. *Journal of Fluid Mechanics*, *856*, 228–256. https://doi.org/10.1017/jfm.2018.695

Seim, H. E., & Gregg, M. C. (1994). Detailed observations of a naturally occurring shear instability. *Journal of Geophysical Research*, *99*(C5), 10049–10073. https://doi.org/10.1029/94JC00168

Simpson, J. H., & Nunes, R. A. (1981). The tidal intrusion front: An estuarine convergence zone. *Estuarine, Coastal and Shelf Science*, *13*(3), 257–266. https://doi.org/10.1016/S0302-3524(81)80024-2

Smyth, W. D. (2003). Secondary Kelvin–Helmholtz instability in weakly stratified shear flow. *Journal of Fluid Mechanics*, *497*, 67–98. https://doi.org/10.1017/S0022112003006591

Smyth, W. D. (2020). Marginal instability and the efficiency of ocean mixing. *Journal of Physical Oceanography*, *50*(8), 2141–2150. https://doi.org/10.1175/JPO-D-20-0083.1

Smyth, W. D., & Carpenter, J. R. (2019). *Instability in geophysical flows* (1st ed.). Cambridge University Press. https://doi.org/10.1017/9781108640084

Smyth, W. D., & Moum, J. N. (2012). Ocean mixing by Kelvin-Helmholtz instability. *Oceanography*, *25*(2), 140–149. https://doi.org/10.5670/oceanog.2012.48

Smyth, W. D., & Moum, J. N. (2013). Marginal instability and deep cycle turbulence in the eastern equatorial Pacific Ocean. *Geophysical Research Letters*, *40*(23), 6181–6185. https://doi.org/10.1002/2013GL058403

Smyth, W. D., Moum, J. N., & Caldwell, D. R. (2001). The efficiency of mixing in turbulent patches: Inferences from direct simulations and microstructure observations. *Journal of Physical Oceanography*, *31*(8), 1969–1992. https://doi.org/10.1175/1520-0485(2001)031⟨1969:TEOMIT⟩2.0.CO;2

Smyth, W. D., Moum, J. N., Li, L., & Thorpe, S. A. (2013). Diurnal shear instability, the descent of the surface shear layer, and the deep cycle of equatorial turbulence. *Journal of Physical Oceanography*, *43*(11), 2432–2455. https://doi.org/10.1175/JPO-D-13-089.1

Staquet, C. (1995). Two-dimensional secondary instabilities in a strongly stratified shear layer. *Journal of Fluid Mechanics*, *296*, 73–126. https://doi.org/10.1017/s0022112095002072

Steinbuck, J. V., Stacey, M. T., McManus, M. A., Cheriton, O. M., & Ryan, J. P. (2009). Observations of turbulent mixing in a phytoplankton thin layer: Implications for formation, maintenance, and breakdown. *Limnology & Oceanography*, *54*(4), 1353–1368. https://doi.org/10.4319/lo.2009.54.4.1353

Taylor, J. R., de Bruyn Kops, S. M., Caulfield, C. P., & Linden, P. F. (2019). Testing the assumptions underlying ocean mixing methodologies using direct numerical simulations. *Journal of Physical Oceanography*, *49*(11), 2761–2779. https://doi.org/10.1175/jpo-d-19-0033.1

Taylor, J. R., & Thompson, A. F. (2023). Submesoscale dynamics in the upper ocean. *Annual Review of Fluid Mechanics*, *55*(1), 103–127. https://doi.org/10.1146/annurev-fluid-031422-095147

Tedford, E. W., Carpenter, J. R., Pawlowicz, R., Pieters, R., & Lawrence, G. A. (2009). Observation and analysis of shear instability in the Fraser River estuary. *Journal of Geophysical Research*, *114*(C11), C11006. https://doi.org/10.1029/2009jc005313

Thorpe, S. A. (1971). Experiments on the instability of stratified shear flows: Miscible fluids. *Journal of Fluid Mechanics*, *46*(2), 299–319. https://doi.org/10.1017/s0022112071000557

Thorpe, S. A. (1973). Experiments on instability and turbulence in a stratified shear flow. *Journal of Fluid Mechanics*, *61*(4), 731–751. https://doi.org/10.1017/S0022112073000911

Thorpe, S. A. (2005). *The turbulent Ocean*. Cambridge University Press.

Thorpe, S. A., & Liu, Z. (2009). Marginal instability? *Journal of Physical Oceanography*, *39*(9), 2373–2381. https://doi.org/10.1175/2009JPO4153.1

Tu, J., Fan, D., Lian, Q., Liu, Z., Liu, W., Kaminski, A., & Smyth, W. (2020). Acoustic observations of Kelvin-Helmholtz billows on an estuarine Lutocline. *Journal of Geophysical Research: Oceans*, *125*(4), e2019JC015383. https://doi.org/10.1029/2019JC015383

Tu, J., Fan, D., Sun, F., Kaminski, A., & Smyth, W. (2022). Shear instabilities and stratified turbulence in an estuarine fluid mud. *Journal of Physical Oceanography*, *52*(10), 2257–2271. https://doi.org/10.1175/JPO-D-21-0230.1

Tu, J., Wu, J., Fan, D., Liu, Z., Zhang, Q., & Smyth, W. D. (2024). Shear instability and turbulent mixing by Kuroshio intrusion into the Changjiang River plume. *Geophysical Research Letters*, *51*(20), e2024GL110957. https://doi.org/10.1029/2024GL110957

Vallis, G. K. (2017). *Atmospheric and Oceanic fluid dynamics: Fundamentals and large-scale circulation* (2nd ed.). Cambridge University Press.

van Haren, H. (2000). Properties of vertical current shear across stratification in the north sea. *Journal of Marine Research*, *58*(3), 465–491. https://doi.org/10.1357/002224000321511115

van Haren, H., & Gostiaux, L. (2010). A deep-ocean Kelvin-Helmholtz billow train. *Geophysical Research Letters*, *37*(3), L03605. https://doi.org/10.1029/2009GL041890

van Haren, H., Gostiaux, L., Morozov, E., & Tarakanov, R. (2014). Extremely long Kelvin-Helmholtz billow trains in the Romanche Fracture Zone. *Geophysical Research Letters*, *41*(23), 8445–8451. https://doi.org/10.1002/2014gl062421

van Haren, H., Maas, L., Zimmerman, J. T. F., Ridderinkhof, H., & Malschaert, H. (1999). Strong inertial currents and marginal internal wave stability in the central north sea. *Geophysical Research Letters*, *26*(19), 2993–2996. https://doi.org/10.1029/1999GL002352

Vladoiu, A., Lien, R.-C., Kunze, E., Ma, B., Essink, S., Yang, Y. J., et al. (2025). Finescale measurements of Kelvin-Helmholtz instabilities at a Kuroshio seamount. *Journal of Physical Oceanography*, *55*(11), 2097–2117. https://doi.org/10.1175/JPO-D-24-0235.1

Waterhouse, A. F., MacKinnon, J. A., Nash, J. D., Alford, M. H., Kunze, E., Simmons, H. L., et al. (2014). Global patterns of diapycnal mixing from measurements of the turbulent dissipation rate. *Journal of Physical Oceanography*, *44*(7), 1854–1872. https://doi.org/10.1175/JPO-D-13-0104.1

Wenegrat, J. O., & McPhaden, M. J. (2015). Dynamics of the surface layer diurnal cycle in the equatorial Atlantic Ocean (0°, 23°W). *Journal of Geophysical Research: Oceans*, *120*(1), 563–581. https://doi.org/10.1002/2014JC010504

Wesson, J. C., & Gregg, M. C. (1994). Mixing at Camarinal sill in the strait of Gibraltar. *Journal of Geophysical Research*, *99*(C5), 9847–9878. https://doi.org/10.1029/94jc00256

Zhu, L., Atoufi, A., Lefauve, A., Taylor, J. R., Lawrence, G. A., Dalziel, S. B., & Linden, P. F. (2023). Stratified inclined duct: Direct numerical simulations. *Journal of Fluid Mechanics*, *969*, A20. https://doi.org/10.1017/jfm.2023.502